
CanViT: Toward Active-Vision Foundation Models

Yohai-Elie Berreby^{1,2} Sabrina Du^{1,2} Audrey Durand^{2,3} B. Suresh Krishna¹

¹McGill University ²Mila - Quebec AI Institute ³Université Laval

me@yberreby.com sabrina.du@mail.mcgill.ca audrey.durand@ift.ulaval.ca
suresh.krishna@mcgill.ca

Abstract

Active computer vision promises efficient, biologically plausible perception through sequential, localized glimpses, but lacks scalable general-purpose architectures and pretraining pipelines. As a result, Active-Vision Foundation Models (AVFMs) have remained unexplored. We introduce **CanViT**, the first task- and policy-agnostic AVFM. CanViT uses scene-relative RoPE to bind a retinotopic Vision Transformer backbone and a spatiotopic scene-wide latent workspace, the *canvas*. Efficient interaction with this high-capacity working memory is supported by Canvas Attention, a novel asymmetric cross-attention mechanism. We decouple *thinking* (backbone-level) and *memory* (canvas-level), eliminating canvas-side self-attention and fully-connected layers to achieve low-latency sequential inference and scalability to large scenes. We propose a label-free active vision pretraining scheme, **policy-agnostic passive-to-active dense latent distillation**: reconstructing scene-wide DINOv3 embeddings from sequences of low-resolution glimpses with randomized locations, zoom levels, and lengths. We pretrain CanViT-B from a random initialization on 13.2 million ImageNet-21k scenes—an order of magnitude more than previous active models—and 1 billion random glimpses, in 166 hours on a single H100. On ADE20K segmentation, a frozen CanViT-B achieves 38.5% mIoU in a single low-resolution glimpse, outperforming the best active model’s 27.6% with 19.5x fewer inference FLOPs and no fine-tuning, as well as its FLOP- or input-matched DINOv3 teacher. Given additional glimpses, CanViT-B reaches 45.9% ADE20K mIoU. On ImageNet-1k classification, CanViT-B reaches 81.2% top-1 accuracy with frozen teacher probes. CanViT generalizes to longer rollouts, larger scenes, and new policies. Our work closes the wide gap between passive and active vision on semantic segmentation and demonstrates the potential of AVFMs as a new research axis.

1 Introduction

Deep Artificial Neural Networks (ANNs) have achieved outstanding performance in a variety of computer vision tasks, and proven valuable to life sciences research as computational models of biological visual processing¹⁻⁷. This practical and scientific success has largely hinged on vision encoders which process individual frames independently and passively, without the ability to reuse previous computation to guide further processing in a recurrent, active, human-like manner.

Unlike most ANNs, humans sample their visual environment by actively and frequently orienting their sensory apparatus towards regions of interest (ROIs), through gaze shifts. This process is inherently sequential, and involves strategic planning^{8,9}, integration of evidence across time in visual working memory^{10,11}, and top-down recurrent feedback—rich conditioning of early visual pathways by signals from higher brain areas, allowing each fixation’s visual information to be processed in a contextually informed manner, based on what was seen earlier¹²⁻¹⁴, rather than *tabula rasa*.

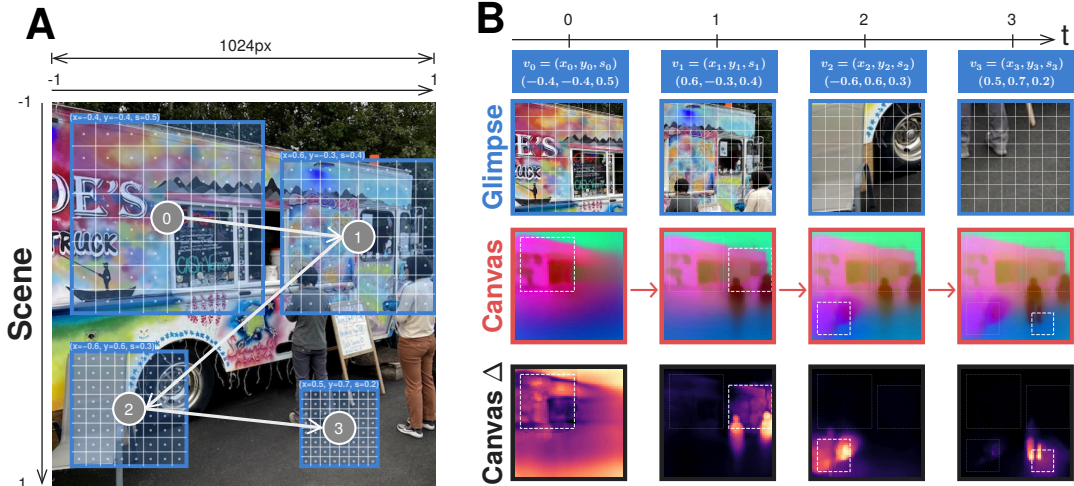


Figure 1: **A CanViT rollout.** We consider a high-resolution scene (A). At each timestep t , CanViT ingests a 128^2 px *glimpse* (B, 1st row), a crop extracted at a *viewpoint* with center $(x_t, y_t) \in [-1, +1]^2$ and scale (zoom level) $s_t \in (0, 1]$. This updates a scene-wide latent representation, the *canvas*, with which CanViT integrates broad context and fine detail from variable-scale glimpses, extrapolates to unobserved regions, and conditions visual processing on a working understanding of the scene. We visualize the canvas via Principal Component Analysis across tokens (B, 2nd row), and canvas updates (Δ) as cosine dissimilarity heatmaps across consecutive timesteps (B, 3rd row).

Various Active Computer Vision (ACV) models have been proposed, drawing inspiration from human vision to process visual scenes through sequential, localized glimpses, in pursuit of biological relevance and computational efficiency^{15–26}. Despite theoretical advantages, active vision models have struggled to match the accuracy, efficiency, flexibility and representational richness of their passive counterparts. This disconnect is particularly striking on dense prediction, which is unsupported by most existing active vision models; the few exceptions^{23,24} lag dramatically behind passive models on standard benchmarks like ADE20K-SceneParse150 segmentation²⁷.

An active vision model can be considered along three axes: making sense of what it sees at a given moment (instantaneous vision); updating a persistent, evolving understanding of the scene, which may in turn inform further processing (memory); and deciding where and at what zoom level to look next (action selection). The first two axes define an observer’s ability to understand, persist, and recall visual inputs, while the last defines its input-selection strategy, or sensory policy. They do not play comparable roles: given perfect instantaneous vision and memory, naive and strategic policies should reach the same accuracy after enough glimpses of a static scene, but no policy can make up for a poor observer. Yet, prior ACV work has primarily focused on action selection^{15,23,24}. Concurrently, passive-vision foundation models like DINOv3²⁸ excel at general-purpose instantaneous vision but lack essential active-vision components, as they have no concept of localized glimpses or memory.

Focusing on the intersection of instantaneous vision and memory, we sought to build an Active-Vision Foundation Model (AVFM): a vision model capable of understanding the spatial and semantic structure of scenes across arbitrary sequences of glimpses, with rich representations that transfer across tasks and viewing policies. Disentangling “how to see in an active-vision setting” from “where to look” frees active vision pretraining from the complexity of Reinforcement Learning (RL) while facilitating real-world deployment, where physical limitations—e.g. a motorized camera’s range of motion and optical zoom levels—may impose additional constraints on viewing policies.

Contributions. We introduce the Canvas Vision Transformer (CanViT), a novel recurrent ViT architecture (Section 4) pretrained with a novel passive-to-active distillation scheme (Section 5). We evaluate a frozen CanViT-B’s zero-shot transfer across tasks, policies, temporal horizons and resolutions (Section 6). Even without fine-tuning, CanViT establishes a new accuracy–efficiency frontier on ADE20K active segmentation while delivering competitive ImageNet-1K performance and strong generalization. Our work introduces AVFMs as a new research axis, empirically validates their potential, and provides a blueprint for future research on general-purpose active vision.

2 Related Work

Deep active vision. Deep active vision models typically process sequences of *glimpses*—fixed- or variable-scale crops extracted from a larger image or video. This line of research traces back to Mnih’s Recurrent Attention Model (RAM)¹⁵, and remained largely confined to simple tasks such as digit recognition^{16,17} until 2019, when Saccader¹⁸ achieved 75% ImageNet-1K top-1 accuracy by introducing an intermediate pretraining step to stabilize learning. GFNet¹⁹ and AdaptiveNN²⁵ later showed that active vision could deliver computational efficiency gains on real-world tasks, although both remained structurally limited to classification and fixed zoom levels.

Dense prediction in active vision. Most active vision architectures cannot produce the scene-wide, spatially dense outputs required for semantic segmentation, depth estimation, and other dense tasks. Among the few exceptions, AME²³ and AdaGlimpse²⁴ both achieve dense prediction through post-hoc expansion of encoder outputs: at each timestep, a MAE-style²⁹ Transformer decoder receives all encoded glimpse tokens with a full grid of learnable mask tokens and performs self-attention over the entire grid to produce scene-wide predictions, becoming intractable at high scene resolutions where active vision may be most appealing. Despite being the active-vision state of the art on the ADE20K segmentation benchmark, these models respectively achieve only 27.6% and 25.7% mIoU.

Dense latent distillation in ViTs. The visuospatial intelligence acquired through extensive self-supervised pretraining can be quickly transferred into randomly-initialized models: DINOv2³⁰ and DINOv3²⁸ distilled their largest model into ViTs of various sizes using the same dataset and the same loss function as during pretraining. Proteus³¹ distilled DINOv2- $\{g,L\}/14$ ³⁰ into a smaller model using $100\times$ less data than during pretraining and a simple loss combining CLS token matching with dense feature matching. Our passive-to-active dense distillation follows a similar philosophy to Proteus, transferring across problem settings rather than across model sizes: we use a passive teacher’s visual world knowledge to teach an active student how to see from arbitrary glimpse sequences.

Cross-attention for dimensionality/computation decoupling. Set Transformer³² introduced cross-attention routing through a compact set of inducing points to avoid quadratic pairwise attention over input tokens, an approach that was popularized by Perceiver models^{33,34} in other contexts, then further generalized by Recurrent Interface Networks (RINs)³⁵. Like RINs, CanViT alternates read and write cross-attention across depth and time, although with external input on the few-token side (backbone) and recurrent state on the many-token side (canvas). Moreover, CanViT’s many-token side forgoes not only self-attention, but also all fully-connected layers: canvas tokens never go through Multi-Layer Perceptrons (MLPs), QKVO projections in cross-attention, or GRU³⁶/LSTM³⁷ recurrent gates.

Latent-space recurrent reasoning. Weight-tied recurrent processing over a fixed external input decouples representational capacity from effective computational depth, enabling improved algorithmic reasoning^{38–42} and flexible test-time compute allocation^{43,44}. This paradigm has recently seen renewed interest, particularly in the Large Language Model (LLM) space^{45,46} and for its ability to produce small yet highly capable models^{41,42}. Such models leverage top-down recurrent feedback to reuse previous computation, rather than losing most of it to ephemeral step-wise outputs. Active vision—and active sensing in general—offers an opportunity to generalize this framework, allowing each weight-tied processing step to benefit from a new perspective on the model’s input or environment in addition to its working understanding of it. CanViT implements this idea with a semantically rich (rather than pixel-like) latent workspace, the *canvas*, which is inexpensively decoded at each timestep and provides top-down recurrent feedback for early layers to build upon.

3 Preliminaries

Definitions: Scenes, Glimpses, Viewpoints. For a timestep $t \in \mathbb{N}$, we consider a bounded 2D *scene*, which can be formally represented as a function $\psi_t : [-1, +1]^2 \rightarrow \mathbb{R}^3$ mapping continuous-valued (x, y) coordinates to RGB triplets. This formulation is compatible with time-varying scenes without a pre-set spatial resolution, e.g. a video feed from a camera with motorized lenses. When the scene is a static image, $\psi_t = \psi_0$ for all timesteps, and ψ_0 simply samples from a pixel grid. We define a *glimpse* as a fixed-resolution crop, extracted at a *viewpoint* $\mathbf{v}_t = (x_t, y_t, s_t)$, where $(x_t, y_t) \in [-1, +1]^2$ is the crop center in scene coordinates and $s_t \in (0, 1]$ is the crop’s *scale*, or half-side-length. That is, the crop spans the scene coordinates $[x_t - s_t, x_t + s_t] \times [y_t - s_t, y_t + s_t]$, covering a fraction s_t^2 of

the scene’s surface area. Regardless of its scale s_t , the crop is resized to a fixed resolution of $H_g \times W_g$ pixels, which determines its information capacity; under that constraint, s_t smoothly controls the tradeoff between spatial coverage and perception of detail.

General-Purpose, Spatially-Grounded Active Vision. An AVFM, in the sense that we describe in the Introduction, should build up a general-purpose understanding of the *scene* through a sequence of *glimpses* that it perceives, allowing each additional processing step to build upon and refine this understanding. This evolving latent representation should be readily decodable into predictions at every timestep, whether for non-spatial, global prediction tasks like object classification or spatially-grounded, dense tasks like semantic segmentation or depth estimation. The latter require explicit architectural handling, as the active vision setting breaks the direct, connectivity-based mapping between input and output feature maps that passive Convolutional Neural Networks (CNNs) and ViTs commonly exploit: glimpses need not be aligned with the scene from which they are extracted.

To address this problem, we introduce the **Canvas Vision Transformer**, or **CanViT** (Section 4), a recurrent vision architecture built around a scene-wide latent representation called the **canvas**.

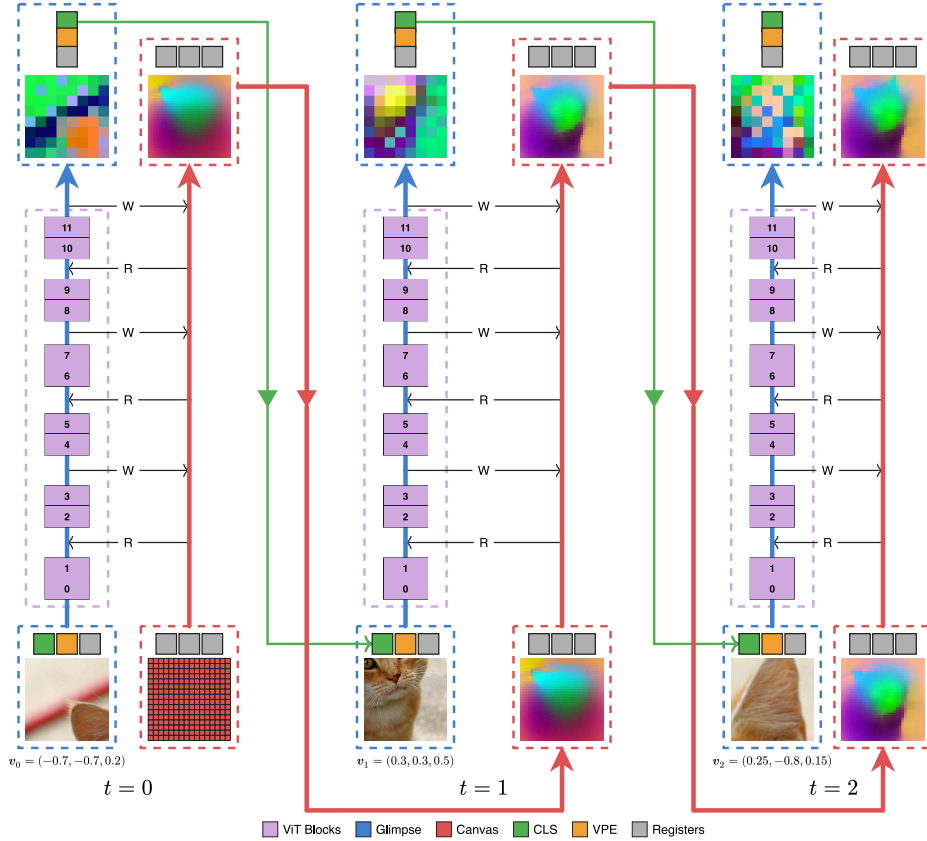


Figure 2: **CanViT architecture diagram.** We adopt a dual-stream structure, equipping a **ViT backbone** (purple, left-hand columns), which processes localized **glimpses** (blue), with a **canvas** (red, right-hand columns), a fine-grained scene-wide spatio-semantic memory. At each timestep t , a glimpse is extracted from a viewpoint $v_t = (x_t, y_t, s_t)$, patchified, and processed through the backbone, alongside a recurrent CLS token and a Viewpoint Encoding (VPE) token. The canvas regularly interacts with the glimpse stream via **Canvas Attention** (Figure 3), alternating between read (R) and write (W) operations to, respectively, condition the backbone’s processing on the canvas and populate the canvas. Both streams are equipped with register tokens⁴⁷.

4 The Canvas Vision Transformer (CanViT)

The CanViT architecture (Figure 2) formulates active-vision processing in a dual-stream manner, as the interaction between a high-capacity memory stream (the *canvas*) and a ViT⁴⁸ backbone’s compact processing stream. These two streams interact bidirectionally through Canvas Attention (Figure 3), an asymmetric cross-attention mechanism which allows the backbone to efficiently pull information from the canvas and send updates to it.

The **backbone stream**, made up of D_{bb} -dimensional tokens, is largely ephemeral. Each glimpse is extracted from the scene at the provided viewpoint, split into 16^2 px patches, and fed to a ViT backbone alongside ephemeral register tokens⁴⁷, a single recurrent CLS token, and a viewpoint encoding (VPE) token derived from the glimpse’s position and zoom level. Since spatial alignment between consecutive patch grids cannot be assumed, as a glimpse may be taken from any position and at any zoom level, patch tokens cannot be directly forwarded across time without destroying their grid structure. Instead, CanViT persists relevant information from each glimpse via the canvas stream.

The **canvas stream**, made up of D_{can} -dimensional tokens, is fully persistent. The canvas acts as a scene-wide spatio-semantic memory, which can function as a cognitive map⁴⁹ of the scene. It comprises a few non-spatial *canvas registers*, which act as a non-spatial memory, and a large $H \times W$ spatial grid of *canvas patches* tiling the $[-1, +1]^2$ scene coordinate space. At the start of each rollout, this grid is broadcasted to the desired size from a single learnable initial patch, enabling the canvas resolution to be set at inference time. Each canvas patch maps onto a fixed scene region, regardless of the current viewpoint, thus allowing direct token-wise decoding into dense predictions and unbroken gradient flow across time. After initialization, the canvas is read from and written to by consecutive Canvas Attention layers, whose outputs are residuals injected into each stream. No MLPs or self-attention layers are applied to canvas tokens, which evolve solely by interacting with the backbone via Canvas Attention Write operations. This restriction is key to CanViT’s efficiency, as the canvas stream is designed to accommodate a much larger number of tokens than the backbone stream.

Scene-Relative Rotary Position Embeddings (SR-RoPE). We compute 2D RoPE^{50,51} from the centers of glimpse patches and canvas patches in the scene’s $[-1, +1]^2$ coordinate system, both in the ViT backbone’s self-attention and in Canvas Attention layers. The positions of glimpse patch centers depend on the current viewpoint, with their relative distances implicitly communicating the viewing scale s_t (zoom): as shown on Figure 1, a zoomed-in glimpse’s patches span a small, tightly-clustered region of the scene coordinate space, while a zoomed-out glimpse’s tokens span a wider region. The positions of canvas patches are constant for any given canvas grid size, since they uniformly tile the scene. Consistent use of scene-relative (SR) coordinates binds the retinotopic backbone stream and the spatiotopic canvas stream with a shared reference frame, while the use of RoPE allows CanViT to generalize well across glimpse and canvas patch grid sizes.

Canvas Attention (Figure 3; pseudocode in Appendix Section B), a mechanism based on cross-attention, enables efficient interaction between CanViT’s relatively small set of glimpse tokens and its much larger set of canvas tokens. We alternate between *Read* and *Write* operations along depth (and, implicitly, time) using a *stride* of 2 ViT blocks in CanViT-B. In a *Read*, backbone tokens query the canvas; in a *Write*, canvas tokens query the backbone. In both cases, the cross-attention output is added back to the querying stream via residual addition. SR-RoPE makes this process spatially aware, allowing Canvas Attention to bind the two streams. Unlike standard cross-attention implementations (e.g. `nn.MultiHeadAttention` in PyTorch⁵², or Flax’s `nnx.MultiHeadAttention` in the JAX ecosystem^{53,54}), Canvas Attention restricts Query, Key, Value and Output (QKVO) projections to one side of the computation (backbone-side tokens), applying only LayerNorm, RoPE (for Queries/Keys) and element-wise residual addition to the other token set (canvas-side tokens).

Asymmetric projections. The glimpse token count N_{bb} must be kept low due to the quadratic cost of the ViT backbone’s self-attention, and it is desirable for the canvas to have high information capacity both *spatially*, by tiling the scene in a fine-grained manner with a large number $H \times W$ of canvas patch tokens (making up the bulk of the N_{can} canvas tokens), and *semantically* at any given position within the scene, with a large canvas embedding dimension D_{can} . This makes the asymmetric design of Canvas Attention highly advantageous, as the FLOP footprint of a single canvas-side projection relative to the Scaled Dot Product Attention (SDPA) call that it accompanies would be:

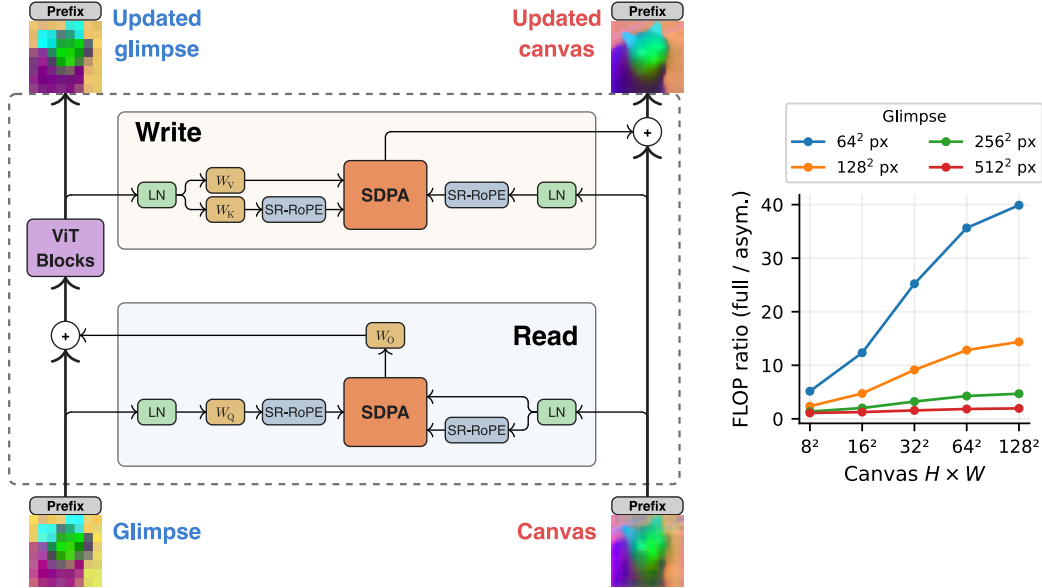


Figure 3: Left: A Canvas Attention round-trip (one Read and one Write) with a zoomed-out, full-scene glimpse ($s = 1$). Right: FLOP savings from eliminating canvas-side projections.

$$\frac{\text{projection FLOPs}}{\text{SDPA FLOPs}} = \frac{2N_{\text{can}}D_{\text{can}}d}{4N_{\text{bb}}N_{\text{can}}d} = \frac{D_{\text{can}}}{2N_{\text{bb}}}, \quad (1)$$

which is a 7.2x ratio with $D_{\text{can}} = 1024$ and $N_{\text{bb}} = 71$ (64 glimpse patches, 5 registers, and CLS + VPE tokens). In CanViT-B, with a 32×32 canvas patch grid, adding canvas-side QKVO projections would increase the cost of each Canvas Attention Read/Write pair from 1.1 to 9.8 GFLOPs. This effect is exacerbated when using smaller glimpses and more canvas tokens (Figure 3, Right).

Viewpoint Encoding (VPE) Token. We supplement SR-RoPE, which distributes the encoding of viewpoint position and scale over glimpse and canvas patches, with a dedicated viewpoint encoding (VPE) token. The VPE token is instantiated at a given glimpse by encoding the current viewpoint (x, y, s) as the triplet $(\frac{x}{s}, \frac{y}{s}, \log s)$, a parameterization with scale invariance, translation invariance, and planar isotropy properties (Appendix Section C). We lift this triplet into backbone embedding space via Random Fourier Features (RFF)⁵⁵, then apply layer normalization⁵⁶ before letting the backbone process it alongside the other glimpse tokens (patches, registers, and recurrent CLS token). The VPE token is meant to facilitate future end-to-end policy learning by allowing the next viewpoint to be decoded from a rich transformation of the current viewpoint; pretraining ablations show it to give a modest boost in reconstruction quality (Table 3 k).

5 Policy-Agnostic Passive-to-Active Dense Latent Distillation

As outlined in the Introduction, an active vision model should (1) make sense of what it sees, (2) integrate observations into a persistent scene representation, and (3) decide where to look next. Here, we ask: how can we teach CanViT (1) and (2) in a task-agnostic, spatially aware, label-free manner, while remaining robust to the choice of policy (3)?

5.1 Passive-to-Active Dense Distillation

A natural pretext task for active-vision pretraining is *scene reconstruction*: training the model to produce a best-guess approximation of the overall scene from a sequence of glimpses. This incentivizes understanding of the spatial and semantic structure of scenes, in order to faithfully extrapolate to unseen regions and details. Since our goal is for CanViT to iteratively build a semantically rich “mental image”, we formulate this reconstruction objective in DINOv3²⁸ latent space, rather than in pixel space like passive Masked Autoencoders (MAEs)²⁹ and some active vision models²⁴.

Teacher. The computer vision community has invested considerable resources into training passive vision foundation models with rich world knowledge and visual intelligence. We build upon these efforts by leveraging the DINOv3²⁸ model family, a modern self-supervised vision model family with excellent high-resolution generalization, whose dense representations deliver state-of-the-art zero-shot transfer to classification, segmentation, depth estimation, and other downstream tasks. We use DINOv3 ViT-B as a *high-resolution scene-wide spatio-semantic teacher*, which produces patch tokens (dense features) and a global CLS token. These highly informative reference embeddings represent an idealized scene understanding for CanViT to match using sequences of cheap, partial glimpses. High-resolution teacher inference is much more computationally intensive than a single CanViT forward pass; however, since the teacher is frozen, we precompute reference features once, storing them for subsequent use across epochs and hyperparameter sweeps (Section D.2).

Target standardization. Teacher features exhibit position-dependent statistics: tokens at different spatial locations have different means and variances. We apply per-position z-score standardization to reconstruction targets, based on mean and variance precomputed independently for each position and embedding dimension from a representative sample of 4096 images.

Decoding. At each timestep t , CanViT produces updated canvas tokens, including canvas patches $C_t \in \mathbb{R}^{H \times W \times D_{\text{can}}}$ and canvas registers, and an updated CLS token $h_t \in \mathbb{R}^{D_{\text{bb}}}$. We apply layer normalization⁵⁶, then decode into DINOv3-space reconstructions via token-wise linear projections:

$$\hat{Z}_t = W_{\text{spatial}} \cdot \text{LayerNorm}(C_t), \quad \hat{z}_t = W_{\text{global}} \cdot \text{LayerNorm}(h_t) \quad (2)$$

Loss. Our loss combines patch-level and CLS-level reconstruction, averaged across space and time:

$$\mathcal{L} = \frac{1}{T} \sum_{t=0}^{T-1} \left[\frac{1}{HW} \|\hat{Z}_t - Z^*\|_F^2 + \|\hat{z}_t - z^*\|^2 \right] \quad (3)$$

5.2 Policy Agnosticism

To keep our model robust to the choice of policy, we implement a rollout randomization scheme.

Dual rollouts. At each pretraining step, we run two independent branches from a freshly-initialized canvas, averaging their losses. These branches and their viewpoint sampling policies are referred to as R-IID and F-IID, and only differ by their treatment of the $t = 0$ viewpoint. The R-IID (Random-then-IID) branch treats all timesteps identically, including $t = 0$, keeping the model robust to arbitrary rollout starts. The F-IID (Full-then-IID) branch always starts with the full-scene zoomed-out viewpoint $(x_0, y_0, s_0) = (0, 0, 1)$, which provides a low-resolution but high-spatial-coverage view of each scene at least once over the course of pretraining. In our ablations, we found the use of 1 F-IID + 1 R-IID branch to accelerate convergence compared to 2 R-IID branches, even when evaluating on held-out data using an R-IID policy (Table 3 h).

Sampling of viewpoint center and scale. For all non-initial timesteps, as well as the $t = 0$ timestep of the R-IID branch, we sample $L^2 \sim \mathcal{U}([L_{\text{min}}^2, L_{\text{max}}^2])$ and set $s = 1 - L$. For a glimpse of scale s , valid centers form a box of half-side-length $1 - s$; we draw (x, y) uniformly within it. The resulting marginal scale density is $p(s) \propto (1 - s)$, favoring smaller, more localized glimpses. We set the minimum glimpse size to $s_{\text{min}} = 0.05$, or 0.25% of the scene’s area.

Rollout length randomization. Backpropagation Through Time (BPTT) over long glimpse sequences would require retaining activations from each forward pass through the backbone, or using gradient checkpointing to mitigate memory footprint growth at the cost of additional backward computation. Additionally, long-horizon backpropagation comes with the risk of vanishing or exploding gradients. Our loss provides *temporally* dense supervision, with per-timestep credit assignment, which allows us to train CanViT with truncated BPTT over chunks of only $K = 2$ glimpses. At each chunk boundary, we stop the rollout with probability $p_{\text{stop}} = 0.5$, resulting in a geometric distribution of chunk counts with an *average* sequence length of $T = K/p_{\text{stop}} = 4$ glimpses while occasionally exposing the model to longer sequences. This scheme ensures sequence length robustness on a constant train-time VRAM footprint, with a modest train-time compute overhead due to the low average sequence length.

6 Experiments

To evaluate our approach’s zero-shot transfer across tasks, policies, temporal horizons and scene resolutions, we pretrain a general-purpose CanViT-B checkpoint. After pretraining, we freeze the resulting weights and conduct linear-probing evaluations on downstream tasks, with various policies (Figure 4). Additional details on evaluation methodology and results are provided in Appendix Section F. We additionally benchmark inference latency to verify that CanViT’s FLOP efficiency translates into wall-clock speedups (Appendix Section I).

Pretraining. We pretrain CanViT-B from a random initialization in just 166 hours on a single H100 using the scheme described in Section 5, sampling approximately 1 billion 128^2 px glimpses from 13.2 million 512^2 px ImageNet-21k^{57,58} scenes. We use a 32×32 canvas patch grid during pretraining. Additional details on pretraining are provided in Appendix Section D and in the code release, with a detailed ablation study in Appendix Section E.

Tasks. We evaluate on ADE20K²⁷ semantic segmentation and ImageNet-1K classification. For ADE20K, we train linear probes to predict segmentation masks directly from canvas tokens. For ImageNet-1K, we assess zero-shot transfer from linear probes trained on DINOv3 ViT-B CLS tokens (Section H), and applied to CanViT-B’s destandardized CLS reconstructions for evaluation.

Policies. To assess CanViT’s ability to generalize across policies and their impact on task performance, we supplement the R-IID and F-IID train-time policies described in Section 5.2 with additional inference-time-only policies. We introduce a **Coarse-to-Fine (C2F)** policy, which traverses a quadtree over the scene, deterministically decreasing the viewpoint scale as the rollout progresses while randomizing the visitation order at each scale. To isolate the effect of processing order, we pair C2F with the **Fine-to-Coarse (F2C)** policy, which reverses C2F viewpoint sequences. For ADE20K, we also introduce an **Entropy-guided** variant of C2F, which greedily selects the highest-uncertainty tile among those that have not yet been visited at a given scale, using the segmentation probe’s per-position class entropy. This image-dependent dynamic policy showcases the ability of the canvas to guide viewpoint selection, even without RL. Lastly, to disentangle the impact of additional recurrent processing from that of ingesting different inputs, we consider a **Repeated Full-Scene** policy, which simply iterates over the $(x, y, s) = (0, 0, 1)$ zoomed-out viewpoint.

6.1 Results

A new frontier on ADE20K active segmentation (Figure 4A). From a single zoomed-out 128^2 px glimpse, a frozen CanViT-B reaches 38.5% mIoU on ADE20K at 15.86 GFLOPs, exceeding its DINOv3 ViT-B/16 teacher even at higher compute (33.2% at 18.38 GFLOPs; Table 5). This surpasses the previous active-vision state of the art, AME (SETR), whose peak ADE20K mIoU of 27.6% requires up to 309 GFLOPs. CanViT’s performance is striking, as AME (SETR) was initialized from the weights of a ViT-L that was specifically trained on ADE20K semantic segmentation⁵⁹, while our model is considerably smaller, trained from a random initialization on a different dataset without task labels, and is evaluated without any task-specific fine-tuning. With the C2F policy and a 64^2 canvas, CanViT-B reaches 45.9% mIoU. Even with a worse-than-random policy (F2C), CanViT-B outperforms prior active vision models on accuracy and efficiency.

Zero-shot generalization across policies, horizons and resolutions (Figure 4B, C). C2F, never seen during training, outperforms both training-time policies on ADE20K from $t = 1$ onward (ADE20K mIoU at $t = 4$: C2F 43.2% vs. F-IID 41.7%; IN1K top-1: C2F 80.8% vs. F-IID 80.1%). Processing order matters: after identical image coverage at $t = 20$, C2F (44.2% mIoU) outperforms F2C (41.1%) on ADE20K; this effect is also present on ImageNet-1k (Figure 4 C). Entropy-guided C2F improves over naive C2F at early timesteps (41.1% vs. 40.2% mIoU at $t = 1$). Performance improves through $T = 21$ glimpses on both tasks, well beyond the average of $T \approx 4$ used during pretraining. Even with a constant input (Repeated Full-Scene), recurrent processing improves mIoU from 38.5% to 40% ($t = 0 \rightarrow 1$), but then declines to 38.2% by $t = 20$, highlighting the importance of diverse viewpoints. Despite training exclusively on 512^2 px scenes with a 32^2 canvas, evaluating CanViT-B’s frozen weights on 1024^2 px scenes with a 64^2 canvas consistently provides an accuracy boost, with the gap widening at longer temporal horizons (+1.2pp at $t = 0$, +1.7pp at $t = 20$; C2F: 45.9% vs. 44.2%).

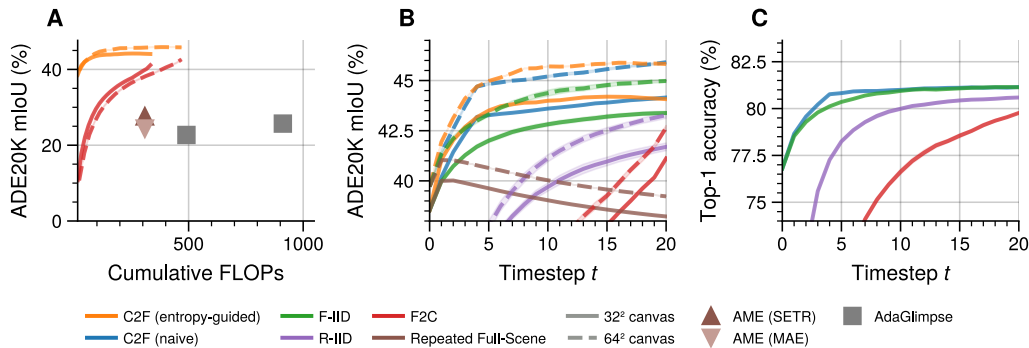


Figure 4: **Linear-probing benchmark results** (frozen CanViT-B). (A) Accuracy–efficiency comparison with prior active models on ADE20K segmentation. (B) Effect of viewing policy and canvas resolution (ADE20K segmentation). (C) Effect of viewing policy (ImageNet-1k classification).

Strong object classification without fine-tuning (Figure 4C). On ImageNet-1k (Table 7), CanViT-B reaches 81.2% top-1 accuracy with the C2F policy and $T = 21$ using frozen teacher probes, outperforming AdaGlimpse’s²⁴ 77.5% and second only to AdaptiveNN’s²⁵ 82.2% among active vision models, despite these baselines relying on end-to-end RL and full-weights task-specific training. Accuracy improves with additional glimpses (C2F: 76.8% \rightarrow 81.2%) and converges faster than on ADE20K, with the gap between F-IID and C2F policies quickly vanishing.

7 Conclusion

CanViT brings the foundation model playbook to active vision, with a general-purpose active-vision model that can be used as-is across tasks and viewing policies. Our results show that pairing a carefully designed active-vision architecture with a highly informative, spatially grounded learning signal is sufficient to dramatically advance the state of the art on active segmentation, narrowing the wide gap between passive and active vision models without relying on complex RL pipelines, extensive pretraining, task-specific full-weights fine-tuning, or initialization with weights from a pretrained encoder. Even with the F2C policy’s worse-than-random viewing order, CanViT outperforms all prior active models on ADE20K active segmentation, validating our assumption that perception, not policy, has been the primary bottleneck in this task. CanViT displays strong zero-shot generalization to unseen structured policies, long viewpoint sequences, and high-resolution scenes and canvas grids, coupled with high computational efficiency at both training and inference, and the ability to derive non-trivial image-dependent viewing policies from first principles using the structure offered by the canvas. Our work highlights the potential of Active-Vision Foundation Models as a promising new paradigm for active vision research, and provides a novel active-vision architecture and an efficient passive-to-active knowledge distillation scheme for practitioners to build upon.

Limitations and future work. While we trained and evaluated CanViT on static natural images, CanViT’s recurrent, constant-memory design and low inference latency even at high scene resolutions make it a natural candidate for adaptation to real-time video processing and, ultimately, embodied active perception. We evaluated CanViT using hand-designed viewing policies without early stopping at inference time; learning viewing policies end-to-end and incorporating confidence-based early stopping are natural next steps to further improve efficiency. Our pretraining scheme currently depends on a pretrained passive teacher; dense latent bootstrapping^{30,60,61} could be adapted to the active-vision setting to remove the dependency. Finally, all results use a single model size (ViT-B), pretrained using a relatively modest compute budget and evaluated with linear probing from frozen weights and, for classification, probes transferred directly from the teacher rather than trained on CanViT features; we expect further gains from using larger models, pretraining them more extensively and evaluating them with full-weights fine-tuning.

References

1. Yamins, D. L. K. *et al.* Performance-Optimized Hierarchical Models Predict Neural Responses in Higher Visual Cortex. *Proceedings of the National Academy of Sciences* **111**, 8619–8624 (2014).
2. Yamins, D. L. K. & DiCarlo, J. J. Using Goal-Driven Deep Learning Models to Understand Sensory Cortex. *Nature Neuroscience* **19**, 356–365 (2016).
3. Schrimpf, M. *et al.* Brain-Score: Which Artificial Neural Network for Object Recognition Is Most Brain-Like?. 407007 (2018) doi:10.1101/407007.
4. Zhuang, C. *et al.* Unsupervised Neural Network Models of the Ventral Visual Stream. *Proceedings of the National Academy of Sciences* **118**, e2014196118 (2021).
5. Bakhtiari, S., Mineault, P., Lillicrap, T., Pack, C. & Richards, B. The Functional Specialization of Visual Cortex Emerges from Training Parallel Pathways with Self-Supervised Predictive Learning. in *Advances in Neural Information Processing Systems* vol. 34 25164–25178 (Curran Associates, Inc., 2021).
6. Mehrer, J., Spoerer, C. J., Jones, E. C., Kriegeskorte, N. & Kietzmann, T. C. An Ecologically Motivated Image Dataset for Deep Learning Yields Better Models of Human Vision. *Proceedings of the National Academy of Sciences* **118**, e2011417118 (2021).
7. Raugel, J. *et al.* Disentangling the Factors of Convergence between Brains and Computer Vision Models. (2025) doi:10.48550/arXiv.2508.18226.
8. Yarbus, A. L. *Eye Movements and Vision*. (Springer US, Boston, MA, 1967). doi:10.1007/978-1-4899-5379-7.
9. Hoppe, D. & Rothkopf, C. A. Multi-Step Planning of Eye Movements in Visual Search. *Scientific Reports* **9**, 144 (2019).
10. Baddeley, A. D. & Hitch, G. Working Memory. vol. 8 47–89 (1974).
11. Melcher, D. Persistence of Visual Memory for Scenes. *Nature* **412**, 401 (2001).
12. Rao, R. P. N. & Ballard, D. H. Predictive Coding in the Visual Cortex: A Functional Interpretation of Some Extra-Classical Receptive-Field Effects. *Nature Neuroscience* **2**, 79–87 (1999).
13. Gilbert, C. D. & Li, W. Top-down Influences on Visual Processing. *Nature Reviews Neuroscience* **14**, 350–363 (2013).
14. Kar, K., Kubilius, J., Schmidt, K., Issa, E. B. & DiCarlo, J. J. Evidence That Recurrent Circuits Are Critical to the Ventral Stream's Execution of Core Object Recognition Behavior. *Nature Neuroscience* **22**, 974–983 (2019).
15. Mnih, V., Heess, N., Graves, A. & Kavukcuoglu, K. Recurrent Models of Visual Attention. in *Advances in Neural Information Processing Systems* vol. 27 (Curran Associates, Inc., 2014).
16. Ba, J., Mnih, V. & Kavukcuoglu, K. Multiple Object Recognition with Visual Attention. in *3rd International Conference on Learning Representations, ICLR 2015, San Diego, CA, USA, May 7-9, 2015, Conference Track Proceedings* (eds. Bengio, Y. & LeCun, Y.) (2015).
17. Ablavatski, A., Lu, S. & Cai, J. Enriched deep recurrent visual attention model for multiple object recognition. in *2017 IEEE Winter Conference on Applications of Computer Vision (WACV)* 971–978 (2017).
18. Elsayed, G., Kornblith, S. & Le, Q. V. Saccader: Improving Accuracy of Hard Attention Models for Vision. in *Advances in Neural Information Processing Systems* vol. 32 (Curran Associates, Inc., 2019).
19. Wang, Y. *et al.* Glance and Focus: A Dynamic Approach to Reducing Spatial Redundancy in Image Classification. in *Proceedings of the 34th International Conference on Neural Information Processing Systems* 2432–2444 (Curran Associates Inc., Red Hook, NY, USA, 2020).
20. Papadopoulos, A., Korus, P. & Memon, N. Hard-Attention for Scalable Image Classification. in *Advances in Neural Information Processing Systems* vol. 34 14694–14707 (Curran Associates, Inc., 2021).
21. Liu, J., Bu, Y., Tso, D. & Qiu, Q. Improved Efficiency Based on Learned Saccade and Continuous Scene Reconstruction From Foveated Visual Sampling. in *The Twelfth International Conference on Learning Representations* (2023).
22. Li, J., Watters, N., Sohn, H. & Jazayeri, M. Modeling Human Eye Movements with Neural Networks in a Maze-Solving Task. in *Proceedings of The 1st Gaze Meets ML Workshop* 98–112 (PMLR, 2023).

23. Pardyl, A., Rypesc, G., Kurzejamski, G., Zielinski, B. & Trzcinski, T. Active Visual Exploration Based on Attention-Map Entropy. in *Proceedings of the Thirty-Second International Joint Conference on Artificial Intelligence, IJCAI 2023, 19th-25th August 2023, Macao, SAR, China* 1303–1311 (ijcai.org, 2023). doi:10.24963/IJCAI.2023/145.
24. Pardyl, A. *et al.* AdaGlimpse: Active Visual Exploration with Arbitrary Glimpse Position and Scale. in *Computer Vision – ECCV 2024* (eds. Leonardis, A. *et al.*) 112–129 (Springer Nature Switzerland, Cham, 2025). doi:10.1007/978-3-031-72664-4_7.
25. Wang, Y. *et al.* Emulating Human-like Adaptive Vision for Efficient and Flexible Machine Visual Perception. *Nature Machine Intelligence* **7**, 1804–1822 (2025).
26. Pourrahimi, M. & Bashivan, P. Emergent Brain-like Representations in a Goal-Directed Neural Network Model of Visual Search. 2025.06.06.658387 (2025) doi:10.1101/2025.06.06.658387.
27. Zhou, B. *et al.* Scene Parsing Through ADE20K Dataset. in *Proceedings of the IEEE Conference on Computer Vision and Pattern Recognition* 633–641 (2017).
28. Siméoni, O. *et al.* DINOv3. (2025) doi:10.48550/arXiv.2508.10104.
29. He, K. *et al.* Masked Autoencoders Are Scalable Vision Learners. in *Proceedings of the IEEE/CVF Conference on Computer Vision and Pattern Recognition* 16000–16009 (2022).
30. Oquab, M. *et al.* DINOv2: Learning Robust Visual Features without Supervision. *Transactions on Machine Learning Research* (2024).
31. Zhang, Y., Ma, X., Bai, Y., Wang, H. & Fu, Y. Accessing Vision Foundation Models via ImageNet-1K. in *The Thirteenth International Conference on Learning Representations* (2025).
32. Lee, J. *et al.* Set Transformer: A Framework for Attention-based Permutation-Invariant Neural Networks. in *Proceedings of the 36th International Conference on Machine Learning* 3744–3753 (PMLR, 2019).
33. Jaegle, A. *et al.* Perceiver: General Perception with Iterative Attention. in *Proceedings of the 38th International Conference on Machine Learning* 4651–4664 (PMLR, 2021).
34. Jaegle, A. *et al.* Perceiver IO: A General Architecture for Structured Inputs & Outputs. in *International Conference on Learning Representations* (2021).
35. Jabri, A., Fleet, D. J. & Chen, T. Scalable Adaptive Computation for Iterative Generation. in *Proceedings of the 40th International Conference on Machine Learning* 14569–14589 (PMLR, 2023).
36. Chung, J., Gulcehre, C., Cho, K. & Bengio, Y. Empirical Evaluation of Gated Recurrent Neural Networks on Sequence Modeling. (2014) doi:10.48550/arXiv.1412.3555.
37. Hochreiter, S. & Schmidhuber, J. Long Short-Term Memory. *Neural Comput.* **9**, 1735–1780 (1997).
38. Dehghani, M., Gouws, S., Vinyals, O., Uszkoreit, J. & Kaiser, L. Universal Transformers. in *International Conference on Learning Representations* (2018).
39. Yang, L., Lee, K., Nowak, R. D. & Papailiopoulos, D. Looped Transformers Are Better at Learning Learning Algorithms. in *The Twelfth International Conference on Learning Representations* (2023).
40. Saunshi, N., Dikkala, N., Li, Z., Kumar, S. & Reddi, S. J. Reasoning with Latent Thoughts: On the Power of Looped Transformers. in *The Thirteenth International Conference on Learning Representations* (2024).
41. Wang, G. *et al.* Hierarchical Reasoning Model. (2025) doi:10.48550/arXiv.2506.21734.
42. Jolicoeur-Martineau, A. Less Is More: Recursive Reasoning with Tiny Networks. (2025) doi:10.48550/arXiv.2510.04871.
43. Graves, A. Adaptive Computation Time for Recurrent Neural Networks. (2017) doi:10.48550/arXiv.1603.08983.
44. Banino, A., Balaguer, J. & Blundell, C. PonderNet: Learning to Ponder. in *8th ICML Workshop on Automated Machine Learning (AutoML)* (2021).
45. Hao, S. *et al.* Training Large Language Models to Reason in a Continuous Latent Space. in *Second Conference on Language Modeling* (2025).
46. Geiping, J. *et al.* Scaling up Test-Time Compute with Latent Reasoning: A Recurrent Depth Approach. (2025) doi:10.48550/arXiv.2502.05171.

47. Darcet, T., Oquab, M., Mairal, J. & Bojanowski, P. Vision Transformers Need Registers. in *The Twelfth International Conference on Learning Representations* (2023).
48. Dosovitskiy, A. *et al.* An Image Is Worth 16x16 Words: Transformers for Image Recognition at Scale. in *International Conference on Learning Representations* (2020).
49. Tolman, E. C. Cognitive Maps in Rats and Men. *Psychological Review* **55**, 189–208 (1948).
50. Su, J. *et al.* RoFormer: Enhanced Transformer with Rotary Position Embedding. *Neurocomputing* **568**, 127063 (2024).
51. Heo, B., Park, S., Han, D. & Yun, S. Rotary Position Embedding for Vision Transformer. in *Computer Vision – ECCV 2024* (eds. Leonardis, A. *et al.*) 289–305 (Springer Nature Switzerland, Cham, 2025). doi:10.1007/978-3-031-72684-2_17.
52. Ansel, J. *et al.* PyTorch 2: Faster Machine Learning Through Dynamic Python Bytecode Transformation and Graph Compilation. in *Proceedings of the 29th ACM International Conference on Architectural Support for Programming Languages and Operating Systems, Volume 2* vol. 2 929–947 (Association for Computing Machinery, New York, NY, USA, 2024).
53. Bradbury, J. *et al.* JAX: composable transformations of Python+NumPy programs. <http://github.com/google/jax> (2018).
54. Heek, J. *et al.* Flax: A neural network library and ecosystem for JAX. <http://github.com/google/flax> (2024).
55. Tancik, M. *et al.* Fourier Features Let Networks Learn High Frequency Functions in Low Dimensional Domains. in *Advances in Neural Information Processing Systems* vol. 33 7537–7547 (Curran Associates, Inc., 2020).
56. Ba, J. L., Kiros, J. R. & Hinton, G. E. Layer Normalization. (2016) doi:10.48550/arXiv.1607.06450.
57. Russakovsky, O. *et al.* ImageNet Large Scale Visual Recognition Challenge. *International Journal of Computer Vision* **115**, 211–252 (2015).
58. Ridnik, T., Ben-Baruch, E., Noy, A. & Zelnik-Manor, L. ImageNet-21K Pretraining for the Masses. (2021) doi:10.48550/arXiv.2104.10972.
59. Zheng, S. *et al.* Rethinking Semantic Segmentation From a Sequence-to-Sequence Perspective With Transformers. in *Proceedings of the IEEE/CVF Conference on Computer Vision and Pattern Recognition* 6881–6890 (2021).
60. Zhou, J. *et al.* iBOT: Image BERT Pre-Training with Online Tokenizer. (2022) doi:10.48550/arXiv.2111.07832.
61. Assran, M. *et al.* Self-Supervised Learning From Images With a Joint-Embedding Predictive Architecture. in *Proceedings of the IEEE/CVF Conference on Computer Vision and Pattern Recognition* 15619–15629 (2023).
62. Touvron, H., Cord, M., Sablayrolles, A., Synnaeve, G. & Jégou, H. Going Deeper With Image Transformers. in *Proceedings of the IEEE/CVF International Conference on Computer Vision* 32–42 (2021).
63. Beyer, L., Hénaff, O. J., Kolesnikov, A., Zhai, X. & Oord, A. van den. Are We Done with ImageNet?. (2020) doi:10.48550/arXiv.2006.07159.

A Interpretability

PCA Visualizations. To visualize grids of high-dimensional glimpse or canvas patch tokens as RGB images (Figure 1, Figure 2, Figure 3, Figure 5), we adopt a similar approach to that of DINOv3²⁸, by performing Principal Component Analysis (PCA) across tokens then mapping groups of three consecutive PCs to RGB. In order to prevent global variance from washing out local detail when visualizing a subset of the canvas, we apply min-max scaling to the resulting RGB channels across the visible region. Unless otherwise specified, we apply this protocol to layer-normalized⁵⁶ tokens, such that each individual token has unit variance and zero mean across its dimensions.

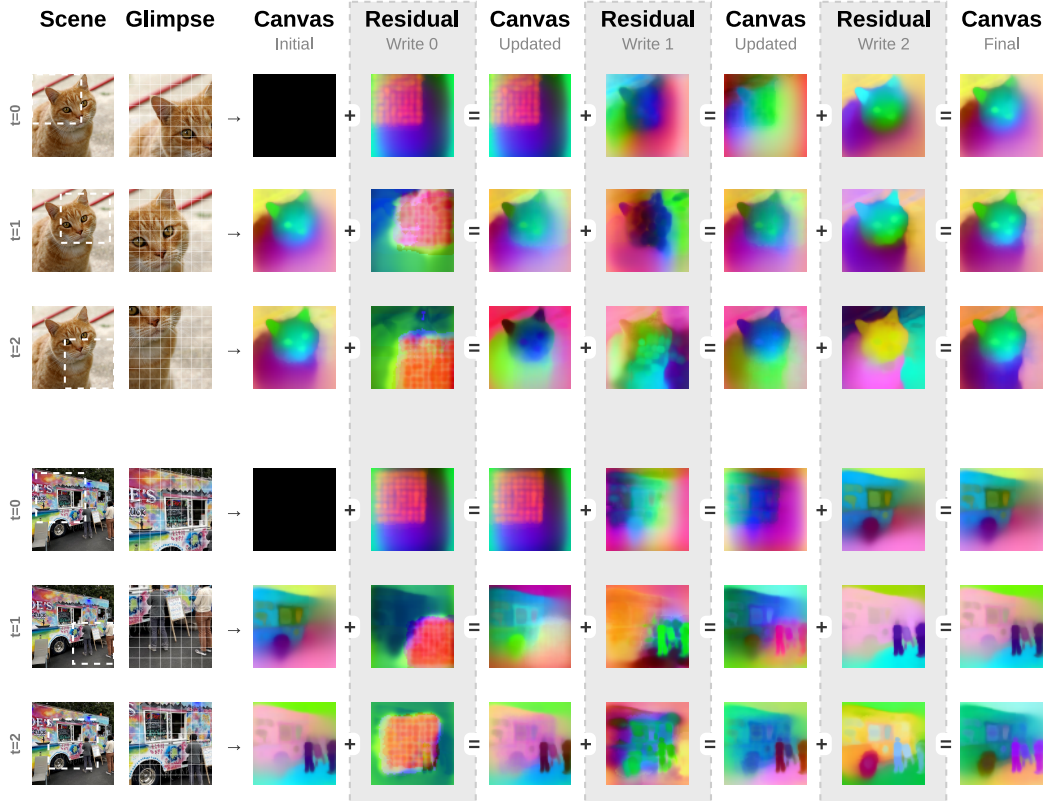


Figure 5: **Canvas updates within and across glimpses.** CanViT sequentially performs multiple Canvas Write Attention operations per glimpse, with each producing a residual that then updates the canvas (Figure 2). To isolate the contribution of individual Write operations, we capture intermediate residuals and canvases after each 128^2 px glimpse, and visualize these snapshots with token-wise PCA. To highlight the individual structure of each snapshot, we compute PCA bases independently for each snapshot. We observe a progression in the spatial structure of residuals as within-glimpse processing unfolds: Write 0 reflects the glimpse grid more than later Writes; Write 1 highlights objects within glimpse borders; and Write 2 seem to refine object boundaries at a scene-level scale.

B Canvas Attention Pseudocode

```
class CanvasAttention(nn.Module):
    def __init__(self, D_q, D_kv):
        self.ln_q = LayerNorm(D_q)
        self.ln_kv = LayerNorm(D_kv)

    # Common template for Reads and Writes
    def forward(self, x_q, x_kv, rope_q, rope_kv):
        q = to_multihead(self.q_map(self.ln_q(x_q)))
        kv = self.ln_kv(x_kv)
        k = to_multihead(self.k_map(kv))
        v = to_multihead(self.v_map(kv))
        q = apply_2d_rope(q, rope_q)
        k = apply_2d_rope(k, rope_kv)
        return self.o_map(from_multihead(sdpa(q, k, v)))

class CanvasAttentionRead(CanvasAttention): # backbone queries canvas
    def __init__(self, D_bb, D_can):
        super().__init__(D_q=D_bb, D_kv=D_can)
        # backbone-side: fully-connected Query and Output projections
        self.q_map = Linear(D_bb, D_can)
        self.o_map = Linear(D_can, D_bb)
        # canvas-side: no-op for Key and Value
        self.k_map = Identity()
        self.v_map = Identity()

class CanvasAttentionWrite(CanvasAttention): # canvas queries backbone
    def __init__(self, D_bb, D_can):
        super().__init__(D_q=D_can, D_kv=D_bb)
        # backbone-side: fully-connected Key and Value projections
        self.k_map = Linear(D_bb, D_can)
        self.v_map = Linear(D_bb, D_can)
        # canvas-side: no-op for Query and Output
        self.q_map = Identity()
        self.o_map = Identity()

# cell centers of uniform RxC grid
# in [-1,+1]^2, shape [R*C, 2]
def grid(R, C):
    ys = (arange(R) + 0.5) / R * 2 - 1
    xs = (arange(C) + 0.5) / C * 2 - 1
    return stack(meshgrid(ys, xs), -1).reshape(R * C, 2)

# Scene-Relative 2D Rotary Position Embeddings
# center in [-1,+1]^2, scale in (0,1]: where and how zoomed-out the viewpoint is
rope_bb = compute_2d_rope(center + scale * grid(H_g, W_g)) # dynamic
rope_can = compute_2d_rope(grid(H_c, W_c)) # fixed

# CanViT alternates reads and writes across depth:
x_bb = blk1(blk0(x_bb))
x_bb = x_bb + read(x_bb, x_can, rope_bb, rope_can)
x_bb = blk3(blk2(x_bb))
x_can = x_can + write(x_can, x_bb, rope_can, rope_bb)
x_bb = blk5(blk4(x_bb))
x_bb = x_bb + read(x_bb, x_can, rope_bb, rope_can)
# ...
```

C Viewpoint Encoding (VPE)

C.1 Definitions: scene, viewpoint, crop

We consider a finite 2D *scene* whose (x, y) coordinates span $[-1, +1]^2$.

We call a **viewpoint** a triplet $(x, y, s) \in \mathcal{V}_{\text{raw}}$ such that the corresponding square crop,

$$[x - s, x + s] \times [y - s, y + s], \quad 4.$$

lies inside $[-1, +1]^2$.

Equivalently,

$$\mathcal{V}_{\text{raw}} = \{(x, y, s) \in \mathbb{R}^2 \times (0, 1] : |x| \leq 1 - s, |y| \leq 1 - s\}. \quad 5.$$

For instance, the viewpoint $(0, 0, 1)$ spans the entire scene; the viewpoint $(0.5, 0.5, 0.5)$ spans the quadrant $[0, 1]^2$; the viewpoint $(2, 2, 0.5)$ is invalid, as its center lies outside of the scene; the viewpoint $(0.5, 0.5, 1)$ is *also* invalid, even though its center lies within the scene, because its borders extend beyond the scene boundaries.

C.2 Finding a scale-invariant representation

While the above representation of a viewpoint as a triplet $(x, y, s) \in \mathcal{V}_{\text{raw}}$ is simple to understand and uniquely defines crops within the scene, it fails to represent an important property: **scale invariance**.

When considering viewpoints as vectors, we would like distances between viewpoints to be **invariant to global rescaling**. In other words, the distance between two side-by-side square crops should be identical regardless of zoom level; at any given location, a 10% difference in zoom level should have an identical effect on viewpoint distance for small and large crops alike. This is not the case in a straightforward (x, y, s) encoding, which becomes artificially insensitive to shifts in position and scale for small crops (i.e. when $s \ll 1$), thus being forced to under-represent fine detail at small scales, leading to loss of information, or over-represent it at large scales, leading to ill-conditioned representations with excessive sensitivity to small perturbations at large scales (when $s \approx 1$).

Formally, we seek a smooth, injective $u : \mathcal{V}_{\text{raw}} \rightarrow \mathcal{V}$ satisfying the following three properties, with d being the Euclidean distance on \mathcal{V} and $q_i = (x_i, y_i, s_i) \in \mathcal{V}_{\text{raw}}$.

Scale invariance:

$$\begin{aligned} \forall c > 0 \text{ with } cq_i = (cx_i, cy_i, cs_i) \in \mathcal{V}_{\text{raw}}, \\ d(u(cq_1), u(cq_2)) = d(u(q_1), u(q_2)) \end{aligned} \quad 6.$$

Same-scale translation invariance:

$$\begin{aligned} \text{With } (x_1, y_1, s), (x_2, y_2, s), (x_1 - x_2, y_1 - y_2, s) \in \mathcal{V}_{\text{raw}}, \\ d(u(x_1, y_1, s), u(x_2, y_2, s)) = d(u(x_1 - x_2, y_1 - y_2, s), u(0, 0, s)) \end{aligned} \quad 7.$$

Isotropy (invariance under valid planar rotations):

$$\begin{aligned} \forall R \in \text{SO}(2), \text{ with } (x_{i,r}, y_{i,r}, s_i) \in \mathcal{V}_{\text{raw}}, \\ d(u(x_{1,r}, y_{1,r}, s_1), u(x_{2,r}, y_{2,r}, s_2)) = d(u(x_1, y_1, s_1), u(x_2, y_2, s_2)) \end{aligned} \quad 8.$$

We find that all of the above properties are satisfied by the embedding $u : \mathcal{V}_{\text{raw}} \rightarrow \mathcal{V} = u(\mathcal{V}_{\text{raw}}) \subset \mathbb{R}^3$ defined by

$$\begin{aligned} u : \mathcal{V}_{\text{raw}} &\rightarrow \mathcal{V} \\ (x, y, s) &\mapsto \left(\frac{x}{s}, \frac{y}{s}, \log s \right) = (u_1, u_2, u_3) \\ u^{-1} : \mathcal{V} &\rightarrow \mathcal{V}_{\text{raw}} \\ (u_1, u_2, u_3) &\mapsto (\exp(u_3)u_1, \exp(u_3)u_2, \exp(u_3)) = (x, y, s). \end{aligned} \quad 9.$$

C.3 Proofs

Lemma: Pairwise distance identity. For $q_i = (x_i, y_i, s_i)$,

$$\begin{aligned} d(u(q_1), u(q_2))^2 &= \|u(q_1) - u(q_2)\|_2^2 \\ &= \left\| \left(\frac{x_1}{s_1} - \frac{x_2}{s_2}, \frac{y_1}{s_1} - \frac{y_2}{s_2}, \log s_1 - \log s_2 \right) \right\|_2^2 \\ &= \left(\frac{x_1}{s_1} - \frac{x_2}{s_2} \right)^2 + \left(\frac{y_1}{s_1} - \frac{y_2}{s_2} \right)^2 + (\log s_1 - \log s_2)^2 \end{aligned} \quad 10.$$

Proof of scale invariance. Let $c > 0$ and $q_i = (x_i, y_i, s_i)$.

$$u(cq_i) = \left(\frac{x_i}{s_i}, \frac{y_i}{s_i}, \log s_i + \log c \right) \quad 11.$$

so

$$u(cq_1) - u(cq_2) = \left(\frac{x_1}{s_1} - \frac{x_2}{s_2}, \frac{y_1}{s_1} - \frac{y_2}{s_2}, (\log s_1 - \log s_2) \right) \quad 12.$$

hence

$$\|u(cq_1) - u(cq_2)\|_2^2 = \|u(q_1) - u(q_2)\|_2^2 \quad 13.$$

■.

Proof of same-scale translation invariance.

$$d(u(x_1, y_1, s), u(x_2, y_2, s))^2 = \left(\frac{x_1 - x_2}{s} \right)^2 + \left(\frac{y_1 - y_2}{s} \right)^2 \quad 14.$$

and

$$\begin{aligned} d(u(x_1 - x_2, y_1 - y_2, s), u(0, 0, s))^2 &= \|u(x_1 - x_2, y_1 - y_2, s) - u(0, 0, s)\|_2^2 \\ &= \left\| \left(\frac{x_1 - x_2}{s}, \frac{y_1 - y_2}{s}, 0 \right) \right\|_2^2 \\ &= \left(\frac{x_1 - x_2}{s} \right)^2 + \left(\frac{y_1 - y_2}{s} \right)^2 \end{aligned} \quad 15.$$

■.

Proof of planar isotropy.

From the pairwise distance identity,

$$d(u(x_1, y_1, s_1), u(x_2, y_2, s_2))^2 = \left\| \left(\frac{x_1}{s_1}, \frac{y_1}{s_1} \right) - \left(\frac{x_2}{s_2}, \frac{y_2}{s_2} \right) \right\|_2^2 + (\log s_1 - \log s_2)^2. \quad 16.$$

For any $R \in \text{SO}(2)$,

$$\begin{aligned}
d(u(R(x_1, y_1), s_1), u(R(x_2, y_2), s_2))^2 &= \left\| \frac{R(x_1, y_1)}{s_1} - \frac{R(x_2, y_2)}{s_2} \right\|_2^2 \\
&\quad + (\log s_1 - \log s_2)^2 \\
&= \left\| R \left(\left(\frac{x_1}{s_1}, \frac{y_1}{s_1} \right) - \left(\frac{x_2}{s_2}, \frac{y_2}{s_2} \right) \right) \right\|_2^2 \\
&\quad + (\log s_1 - \log s_2)^2 \\
&= \left\| \left(\frac{x_1}{s_1}, \frac{y_1}{s_1} \right) - \left(\frac{x_2}{s_2}, \frac{y_2}{s_2} \right) \right\|_2^2 \\
&\quad + (\log s_1 - \log s_2)^2,
\end{aligned} \tag{17}$$

where the second equality uses linearity of R , and the third uses orthogonality $\|Rv\|_2 = \|v\|_2$ for all $v \in \mathbb{R}^2$.

Therefore $d(u(R(x_1, y_1), s_1), u(R(x_2, y_2), s_2)) = d(u(x_1, y_1, s_1), u(x_2, y_2, s_2))$. ■

D CanViT-B Pretraining Details

D.1 Hyperparameters

Table 1: CanViT-B architecture.

Hyperparameter	Value
Backbone	ViT-B/16
Backbone embedding dim	768
Backbone registers (ephemeral)	5
Glimpse patch size	16^2 px
Canvas embedding dim	1024
Canvas registers (persistent)	16
Canvas Attention heads	8
Canvas Attention head dim.	128
Canvas Attention R/W stride	2
RoPE base period	100
RoPE precision	float32
VPE token	Enabled
VPE RFF ⁵⁵ standard deviation σ	1

Table 2: CanViT-B pretraining hyperparameters.

Hyperparameter	Value	Hyperparameter	Value
Optimizer	AdamW	Dataset	ImageNet-21k
Initial learning rate	1.00×10^{-7}	IN21K Version	winter21_whole
Peak learning rate	4.00×10^{-4}	Preprocessing	Resize(512) + CenterCrop
LR schedule	Warmup \rightarrow Const.	Data augmentation	None
LR warmup steps	100,000	Scene resolution	512^2 px (1024 patches)
Weight decay	1×10^{-4}	Glimpse resolution	128^2 px (64 patches)
Gradient clipping	1.0 max norm	Batch size	64 scenes
AdamW β_1, β_2	0.9, 0.999	Total training steps	2.00×10^6
TBPTT chunk size	$K = 2$ glimpses	Min scale	0.05 (0.25% of area)
Stop prob.	$p_{\text{stop}} = 0.5$	Forward precision	AMP bfloat16
Rollouts per step	1 F-IID + 1 R-IID	ViT LayerScale init.	1×10^{-5}

D.2 Teacher Feature Pre-computation

To eliminate the repeated cost of running the teacher’s forward pass during training, we precompute DINOv3 ViT-B features for all 13.2M ImageNet-21k images at 512×512 resolution. Images are processed without augmentation (resize shortest side to 512px, center crop).

Features are stored in float16 and organized into shards of 4096 images each. Each shard contains whole-scene dense patch features and CLS tokens, both obtained after DINOv3’s final LayerNorm.

We pre-shuffle shards during dataset export, enabling us to process the shards themselves sequentially during pretraining. This strategy enables high-bandwidth streaming from networked storage, without incurring the high cost of a random data access pattern.

D.3 Numerical precision considerations

The use of mixed-precision training is critical for efficiency, but comes with numerical correctness considerations, particularly in long-horizon scenarios.

Over the course of this project, we encountered several subtle correctness issues, which only led to meaningful regressions after several hundred thousand steps of pretraining.

For safe CanViT pretraining with minimal performance impact, we recommend the following:

- Keep the canvas in `float32` as it accumulates updates across time and depth.
- Keep all coordinate-related components in `float32`: grid coordinates, RoPE computations, VPE token projection matrix and computation (if enabled).
- Allow other operations, including SDPA operations and learned projection layers, to be performed in `bfloat16`, following standard autocast operator rules.
- Perform the backward pass outside of the AMP region, setting `backward_pass_autocast="off"` accordingly when using `torch.compile`.

We expect careful precision handling to be especially important when training viewing policies end-to-end with RL on top of CanViT.

D.4 Availability of code and weights

We release a reference PyTorch implementation of the CanViT architecture and HuggingFace-compatible pretrained weights at <https://github.com/m2b3/CanViT-PyTorch>.

E Pretraining Ablations

Table 3: **Ablation study.** Δ columns: % change in per-position cosine similarity between canvas reconstruction and DINOv3 teacher features at $t = 9$ (after 10 R-IID glimpses), evaluated on 2,000 held-out ADE20K scenes. Negative = worse than baseline. Sp. = dense (patch-level); CLS = CLS-token. Absolute values and 95% CI in Table 4. Training loss curves in Figure 6.

Variant	Params	GFLOPs	Δ Sp. Cos	Δ CLS Cos
CanViT-B (baseline)	95.2M	15.5	ref	ref
a $D_{\text{can}} = 256$, asymmetric ($n_h = 2$)	88.1M	13.1	-12.0%	-2.1%
b $D_{\text{can}} = 256$, + QKVO ($n_h = 2$)	88.8M	14.8	-11.7%	-1.7%
c $D_{\text{can}} = 384$, + QKVO ($n_h = 3$)	91.0M	17.2	-5.8%	-1.1%
d No canvas reads	90.4M	13.9	-6.5%	-8.0%
e RW stride = 6 (1R / 1W)	88.8M	13.4	-4.1%	-6.0%
f No dense supervision	95.2M	15.5	-98.8%	-9.0%
g No F-IID, $1 \times$ R-IID	95.2M	15.5	-9.4%	-16.3%
h No F-IID, $2 \times$ R-IID	95.2M	15.5	-5.3%	-9.4%
i No BPTT ($K = 1$)	95.2M	15.5	-3.8%	-7.5%
j $D_{\text{bb}} = 384$ (= ViT-S backbone)	26.4M	5.7	-8.5%	-21.2%
k No VPE token	95.2M	15.3	-0.2%	-0.3%

To assess the influence of our most important design choices at the level of architecture and pretraining, we conducted an ablation study using short pretraining runs. For our ablation baseline and each ablated variant, we allocated slightly over 10% of our flagship checkpoint’s pretraining compute, adjusting the learning rate warmup period accordingly.

We report training loss curves on Figure 6, disaggregated by reconstruction target (patch/CLS) and by policy (R-IID/F-IID). As our chosen step count results in slightly more than 1 epoch on the 13.2 million ImageNet-21K images in our pretraining dataset, these training curves are representative of the model’s generalization capabilities.

To quantify generalization, we evaluate each ablation variant on held-out ADE20K validation images by measuring cosine similarity between the canvas reconstruction and DINOv3 teacher features under the R-IID policy. We report the relative change compared to baseline on Table 3, alongside per-glimpse computational footprint and parameter count. Absolute values with confidence intervals are in Table 4.

Capacity–expressiveness trade-offs. The removal of canvas-side QKVO projections is key to the low overhead of Canvas Attention. On any given training or inference budget, this allows for more frequent canvas–backbone interactions, a larger canvas embedding dimension (semantic resolution), and the use of more canvas tokens (spatial resolution). However, at fixed canvas dimensionality, the ablation of these projections reduces the expressiveness of each individual cross-attention operation. To assess the well-foundedness of this trade-off, we reduced canvas dimensionality from $D_{\text{can}} = 1024$ to $D_{\text{can}} = 256$, leading to a dramatic drop in patch reconstruction quality (−12.0%, Table 3 a). Re-introducing canvas-side QKVO projections in a FLOP-matched manner forces the use of a small canvas, resulting in a loss of per-position information capacity and a failure to rescue reconstruction quality via increased expressiveness (−11.7% and −5.8% respectively, Table 3 b, Table 3 c).

Frequency and directionality of canvas–backbone interaction. CanViT interleaves Canvas Attention Read/Write operations along depth. In CanViT-B, this corresponds to 3 reads and 3 writes per glimpse (R/W stride of 2), evenly spread across its ViT-B backbone’s 12 Transformer blocks. Write operations are required in order to update the canvas and produce dense outputs. In contrast, Read operations can be readily ablated; doing so results in a large drop in both patch-level (−6.5%) and CLS-level (−8.0%) reconstruction quality (Table 3 d). This highlights the benefit of canvas-to-backbone communication, which underpins top-down recurrent feedback across timesteps, indirect canvas-to-canvas interaction via the backbone, and generally allows backbone-side computation to benefit from the high-capacity workspace constituted by the canvas. When increasing the R/W stride from 2 to 6 Transformer blocks, which results in just 1 read and 1 write per glimpse, we observe a similar yet slightly less pronounced effect (−4.1%, Table 3 e). Together, these results show the benefits of frequent, bidirectional Canvas Attention operations, and point at the importance of within-glimpse canvas refinement and contextually-aware backbone computation.

Dense latent supervision. Omitting dense supervision is contrary to the goal of using a frozen CanViT’s canvas features for dense tasks. However, this objective-level intervention has no effect on the model’s architecture or raw expressiveness, and could theoretically enhance CLS reconstruction by allowing the model’s representations to be specialized for this purpose, rather than requiring them to support both CLS-level and patch-level reconstruction. In our ablation study, the reverse was true (−9.0%, Table 3 f), showing that the additional information provided by this highly informative, spatially-grounded objective can improve performance in non-spatial tasks even without a separate non-spatial fine-tuning phase.

F-IID rollouts. During pretraining, we average losses and gradients across two rollouts that start from a random (R-IID) or full-scene zoomed-out (F-IID) viewpoint for each scene. The inclusion of a F-IID rollout ensures that at least one glimpse has full spatial coverage and that the full-scene viewpoint, ($x = 0, y = 0, s = 1$), can be seen during training. Simply removing the F-IID rollout (−9.4% spatial, Table 3 g) dramatically slows down the decrease of *the R-IID loss*; however, this also halves the total number of glimpses per optimizer step. To control for this, we trained a second variant that replaces the F-IID rollout with a second R-IID rollout, preserving the total number of glimpses per step (Table 3 h). The controlled variant still incurs a substantial degradation (−5.3% spatial, −9.4% CLS), confirming that the full-scene viewpoint itself is beneficial, beyond its contribution as an additional rollout.

Temporal credit assignment. CanViT uses the smallest possible truncated BPTT chunk size, $K = 2$, in order for gradient updates to take into account a glimpse and its successor. Setting $K = 1$ roughly halves the backward-pass memory footprint, but eliminates gradient flow across time altogether. Given temporally-dense supervision and highly-informative canvas tokens, it may still be possible to obtain meaningful results with $K = 1$, as the model learns to greedily produce a best-guess reconstruction at each timestep, which incidentally produces an informative canvas for the next timestep to reuse. In this ablation, we also decrease the stop probability from 0.5 to 0.25 to keep the expected number of glimpses per optimizer step comparable. We find that removing BPTT (Table 3 i) degrades both spatial (-3.8%) and CLS (-7.5%) reconstruction, indicating that even minimal temporal gradient flow ($K = 2$) contributes meaningfully to learning.

Backbone embedding dimension. Reducing the backbone embedding dimension from $D_{bb} = 768$ to $D_{bb} = 384$ is exactly equivalent to using a ViT-S backbone, rather than ViT-B. This results in the largest drop in parameter count, per-glimpse computational footprint, and CLS reconstruction quality (-21.2%) across all ablations. However, the impact of a narrower backbone on patch (spatial) reconstruction (-8.5%), while significant, remains lower than that of several other ablations.

VPE token. Among all considered ablations, the removal of the VPE token had the lowest impact across both policies and both loss types (-0.2% spatial, -0.3% CLS; Figure 6, Table 3 k).

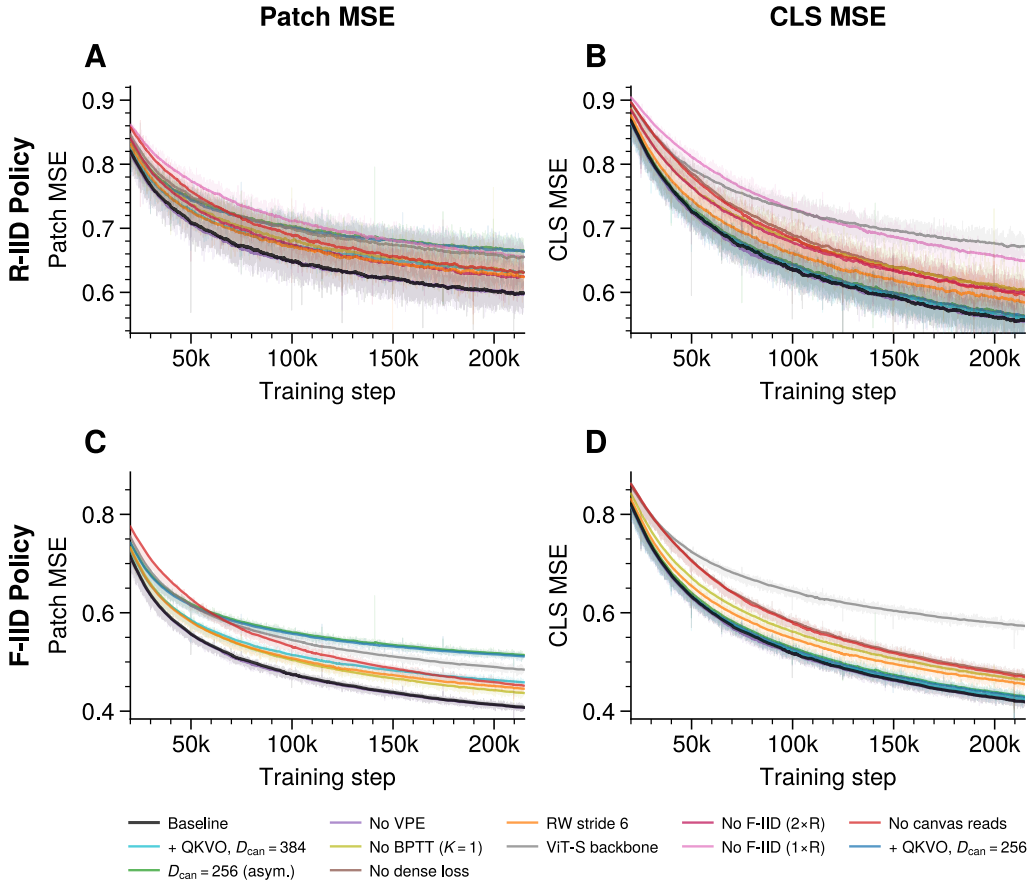


Figure 6: **Ablation pretraining loss curves (ImageNet-21k).** 2×2 grid: rows = policy (R-IID Policy, F-IID Policy), columns = loss component (Patch MSE, CLS MSE). Bold line: EMA-smoothed ($\alpha = 0.01$) over logged per-batch values; faint overlay: pre-EMA values. 11 + 1 variants (baseline + 11 ablations). See also: Table 3

Table 4: **Ablation reconstruction quality (supplementary)**. Per-position cosine similarity ($\%$, $\times 100$) between CanViT canvas reconstruction and DINOv3-B teacher features on held-out ADE20K validation images (2,000 scenes). Shown as 95% bootstrap CI range where $n > 1$; point estimate otherwise. Sp. = spatial (patch-level), CLS = CLS-token. $t = 0$: after one R-IID glimpse; $t = 9$: after 10 R-IID glimpses. Relative changes (Δ) in Table 3.

Variant	$t = 0$		$t = 9$	
	Sp.	CLS	Sp.	CLS
CanViT-B (baseline)	47.2–47.6	46.7–47.3	71.3–71.4	69.6–69.7
$D_{\text{can}} = 256$, asymmetric ($n_h = 2$)	42.7–43	46.1–46.4	62.7–62.8	68.1–68.2
No BPTT ($K = 1$)	46.1–46.5	45.2–45.6	68.6–68.7	64.4–64.5
No dense supervision	0.9–0.9	43.3–43.5	0.9–0.9	63.3–63.5
No F-IID, $1 \times$ R-IID	43.3–43.7	39.9–40.2	64.6–64.7	58.2–58.4
No F-IID, $2 \times$ R-IID	45–46	42.8–43.8	67.6–67.6	63.1–63.2
No canvas reads	45.3–45.9	44.3–45.1	66.7–66.7	64–64.2
No VPE token	46.6–47.1	46–46.6	71.1–71.3	69.4–69.5
$D_{\text{can}} = 256$, + QKVO ($n_h = 2$)	42.6–43.2	45.8–46.6	63–63	68.4–68.5
$D_{\text{can}} = 384$, + QKVO ($n_h = 3$)	44.4–44.9	45.5–46.3	67.1–67.3	68.8–68.9
RW stride = 6 (1R / 1W)	45–45.2	44.1–44.4	68.4–68.5	65.4–65.5
$D_{\text{bb}} = 384$ (= ViT-S backbone)	42.9–43.3	37.7–38	65.3–65.3	54.8–54.9

F Evaluation Details

F.1 Viewing Policies

Full-i.i.d. (F-IID) begins with a full-scene viewpoint ($s = 1$) then samples i.i.d. random crops. Encountered during training (Section 5).

Random-i.i.d. (R-IID) samples i.i.d. random crops at all timesteps, including $t = 0$. Encountered during training.

Coarse-to-Fine (C2F) traverses a quadtree over the scene from coarse to fine. At level $\ell \geq 0$, the viewpoint scale is $s_\ell = 2^{-\ell}$, tiling the scene into a $2^\ell \times 2^\ell$ grid of non-overlapping crops. Let V_ℓ denote the ordered set of viewpoints at level ℓ ; within each level, we visit tiles in a random order $\sigma_\ell(V_\ell)$ (where σ_ℓ is an independent random permutation). The full sequence is the concatenation $V_0, \sigma_1(V_1), \sigma_2(V_2), \dots$, truncated to the glimpse budget T . Novel at inference time.

Fine-to-Coarse (F2C) the reverse of C2F—starts from the finest level and progresses toward coarser views. After identical image coverage, the C2F vs. F2C comparison isolates the effect of processing order.

Entropy-guided C2F a variant of C2F that prioritizes informative regions at each scale level. Rather than visiting tiles in random order, we rank them by the Shannon entropy of the per-position class distribution predicted by the segmentation probe, visiting high-entropy (uncertain) tiles first. This is a zero-shot, image-dependent policy requiring no additional training. Only applicable to ADE20K (requires the segmentation probe).

Repeated Full-Scene repeats the viewpoint $(x, y, s) = (0, 0, 1)$ at every timestep. Serves as a recurrence-only control: any improvement over $t = 0$ must come from iterative canvas refinement with a fixed input, not from observing new regions.

F.2 Decoding Pipeline

For **segmentation**, linear probes operate on canvas patches (excluding registers), bypassing the pre-training reconstruction head W_{spatial} . For **classification**, CanViT’s recurrent CLS token is projected into DINOv3 feature space via the pretraining head W_{global} (Section 5), then destandardized to invert the per-position z-score normalization applied during training. This places the prediction in the original DINOv3 CLS space, allowing direct reuse of a linear probe trained on DINOv3 ViT-B features—making classification a zero-shot transfer from the teacher’s representation space. In both cases, CanViT’s weights are frozen; only the downstream linear probe is task-specific.

F.2.1 ADE20K Segmentation

For ADE20K²⁷ linear probing, we adopt a similar pipeline to DINOv3²⁸, with one notable difference: we do not use sliding-window inference for non-square images. During evaluation, we resize all images directly to a square target resolution (e.g. 512×512), without aspect-ratio preservation. For a fair comparison, we apply this evaluation preprocessing identically to CanViT and DINOv3 probes. Results at higher resolutions (e.g. 1024×1024) use the same protocol at the corresponding resolution.

We train linear probes (LayerNorm + Dropout + BatchNorm + Conv 1×1 , dropout 0.1) for 40,000 steps with AdamW (peak learning rate 3×10^{-4} , weight decay 10^{-3}), using a warmup-cosine schedule (1,500-step warmup), batch size 16, random resized crop with scale range $[0.5, 2.0]$, and random horizontal flips. During ADE20K probe training, we considered sequences of $T = 10$ timesteps; during inference, we used them on sequences of up to $T = 21$ timesteps.

F.2.2 ImageNet-1k Classification

We evaluate on ImageNet-1k⁵⁷ validation. Images are preprocessed by resizing the shortest side to 512 pixels followed by a center crop. As described above, CanViT’s predicted CLS embeddings are destandardized and then passed through a linear probe that was trained on DINOv3 features directly

—CanViT’s backbone is never exposed to classification labels. We report top-1 accuracy across up to $T = 21$ viewpoints.

F.3 ImageNet-1K Probe Training

Because DINOv3 shipped pretrained ImageNet-1k classification heads only for the 7B-parameter flagship model, we trained and released our own linear probes for all five smaller ViT variants. Full details on the probe training methodology and results are provided in Appendix Section H.

Table 5: **Passive-vision comparison: ADE20K mIoU at $t = 0$ (single full-scene glimpse, no recurrence).** CanViT-B vs. DINOv3 ViT-B/16 and ViT-S/16 at various input and output resolutions. All models use frozen features with a linear segmentation probe.

Model	Input	Feat. grid	GFLOPs	mIoU (%)
DINOv3 ViT-S/16	128 px	8×8	3.06	25.2
DINOv3 ViT-S/16	192 px	12×12	6.83	32.3
DINOv3 ViT-S/16	256 px	16×16	12.51	36.9
DINOv3 ViT-S/16	512 px	32×32	63.9	43.3
DINOv3 ViT-B/16	128 px	8×8	11.98	28.8
DINOv3 ViT-B/16	144 px	9×9	14.99	31
DINOv3 ViT-B/16	160 px	10×10	18.38	33.2
DINOv3 ViT-B/16	192 px	12×12	26.32	35.9
DINOv3 ViT-B/16	512 px	32×32	215.21	47.2
CanViT-B (t=0, full scene)	128 px	8×8	13.84	29.3
CanViT-B (t=0, full scene)	128 px	16×16	14.25	35.4
CanViT-B (t=0, full scene)	128 px	32×32	15.86	38.5
CanViT-B (t=0, full scene)	128 px	64×64	22.34	39.7

Table 6: **ADE20K mIoU (%) by policy and timestep ($T = 21$)**. Frozen CanViT-B, linear probe (LayerNorm + Dropout + BatchNorm + Conv1×1). 124 eval runs across 12 configurations. n = independent eval runs; 95% bootstrap CI when $n \geq 2$. Res. = scene px / canvas grid². **Bold** = best across all policies at that timestep.

Policy	Res.	n	G/step	$t = 0$	$t = 1$	$t = 2$	$t = 3$	$t = 4$	$t = 9$	$t = 16$	$t = 20$
C2F	512/32 ²	9	15.9	38.5 ±0	40.2 ±0.1	41.4 ±0.06	42.4 ±0.06	43.2 ±0.03	43.5 ±0.04	44 ±0.04	44.2 ±0.04
Entropy C2F	512/32 ²	9	15.9	38.5 ±0	41.1 ±0	42 ±0	42.7 ±0	43.2 ±0	43.9 ±0	44.2 ±0	44.1 ±0
F-IID	512/32 ²	9	15.9	38.5 ±0	40 ±0.07	40.7 ±0.09	41.3 ±0.09	41.7 ±0.1	42.7 ±0.1	43.3 ±0.09	43.4 ±0.08
R-IID	512/32 ²	9	15.9	18.2 ±0.28	26.1 ±0.47	30.7 ±0.3	33.5 ±0.22	35.3 ±0.17	39.3 ±0.19	41.2 ±0.21	41.7 ±0.19
F2C	512/32 ²	9	15.9	10.7 ±0.19	17.8 ±0.16	22.1 ±0.24	25.2 ±0.2	27.6 ±0.15	34.1 ±0.16	38.4 ±0.11	41.1 ±0.08
Rep. full	512/32 ²	3	15.9	38.5 ±0	40 ±0	40 ±0	39.9 ±0	39.8 ±0	39.1 ±0	38.5 ±0	38.2 ±0
C2F	1024/64 ²	9	22.3	39.7 ±0	41.4 ±0.15	42.6 ±0.11	43.7 ±0.06	44.7 ±0.06	45.1 ±0.05	45.6 ±0.05	45.9 ±0.04
Entropy C2F	1024/64 ²	5	22.3	39.7 ±0	41.9 ±0	43.1 ±0	44.1 ±0	44.7 ±0	45.6 ±0	45.9 ±0	45.8 ±0
F-IID	1024/64 ²	7	22.3	39.7 ±0	41.3 ±0.1	42.1 ±0.11	42.6 ±0.13	43 ±0.12	44.2 ±0.13	44.8 ±0.09	45 ±0.07
R-IID	1024/64 ²	9	22.3	18.2 ±0.5	26.9 ±0.43	31.6 ±0.33	34.5 ±0.27	36.4 ±0.3	40.7 ±0.2	42.7 ±0.14	43.3 ±0.15
F2C	1024/64 ²	9	22.3	10.7 ±0.25	17.9 ±0.16	22.8 ±0.26	26.1 ±0.21	28.6 ±0.2	35.4 ±0.16	39.9 ±0.14	42.7 ±0.11
Rep. full	1024/64 ²	2	22.3	39.7 ±0	41 ±0	41 ±0	40.9 ±0	40.8 ±0	40.1 ±0	39.5 ±0	39.2 ±0

Table 7: **ImageNet-1k top-1 accuracy (%) by policy and timestep**. Frozen CanViT-B with linear classification probe (zero-shot transfer from DINOv3). Bold = best policy at each timestep. ± 95% bootstrap CI ($n = 5$ runs).

Policy	$t = 0$	$t = 1$	$t = 2$	$t = 3$	$t = 4$	$t = 5$	$t = 9$	$t = 15$	$t = 20$
C2F (naive)	76.8 ±0	78.66 ±0.03	79.57 ±0.02	80.21 ±0.03	80.77 ±0.02	80.82 ±0.03	80.97 ±0.04	81.11 ±0.04	81.15 ±0.02
F2C	32.25 ±0.12	48.98 ±0.15	58.38 ±0.09	64.24 ±0.14	68.11 ±0.1	70.76 ±0.06	75.95 ±0.11	78.55 ±0.1	79.77 ±0.02
F-IID	76.8 ±0	78.53 ±0.05	79.29 ±0.05	79.79 ±0.05	80.12 ±0.04	80.36 ±0.01	80.86 ±0.03	81.08 ±0.04	81.14 ±0.04
R-IID	47.62 ±0.07	65.14 ±0.19	72.33 ±0.07	75.59 ±0.1	77.26 ±0.04	78.25 ±0.06	79.84 ±0.08	80.43 ±0.05	80.59 ±0.03

G FLOP Counting

We compute all FLOP counts analytically, counting each multiply-add as two floating-point operations^{48,62}.

Table 8: Notation used throughout this section.

Symbol	Meaning
n	Sequence length (number of tokens)
n_q, n_{kv}	Query and key/value sequence lengths
N_p	Number of patches
d	Embedding dimension
c_{in}, c_{out}	Input and output channel counts
L	Number of Transformer blocks (depth)
T	Number of glimpses (timesteps)
g	Patches per glimpse
p	Patch size (pixels per side)
H, W	Convolution spatial input size
k	Convolution kernel size (pixels per side)

G.1 Primitives

Table 9 lists the FLOP formulas for each primitive operation. Linear, LayerNorm, GELU, and RoPE_apply are per-token costs; in all formulas below they are multiplied by the relevant token count. Softmax counts five operations per element (max, subtract, exp, sum, divide). GELU assumes the tanh-approximation polynomial (≈ 8 FLOPs per element). LayerNorm counts mean, variance, normalize, scale, and shift (5 FLOPs per element). PatchEmbed is a Conv2d with $c_{in} = 3$ (RGB). Bias additions and residual connections are considered negligible.

Table 9: Primitive operation FLOP formulas. Per-token costs are multiplied by the token count in all composed formulas.

Operation	FLOPs (per token)
Linear(d_{in}, d_{out})	$2d_{in}d_{out}$
LN(d)	$5d$
GELU(d)	$\approx 8d$
RoPE_apply (d)	$4d$
Operation	FLOPs (total)
SDPA(n_q, n_{kv}, d)	$4n_qn_{kv}d$
Softmax(n_q, n_{kv})	$5n_qn_{kv}$
Conv2d(H, W, c_{in}, c_{out}, k)	$2HWc_{in}c_{out}k^2$
PatchEmbed(N_p, p, d)	$2N_pp^2 \cdot 3 \cdot d$

G.2 ViT Transformer Block

$$\begin{aligned}
\text{ViTBlock}(n, d) = & n \cdot \text{LN}(d) + n \cdot \underbrace{\text{Linear}(d, 3d)}_{W_{QKV}} + \text{SDPA}(n, n, d) + n \cdot \underbrace{\text{Linear}(d, d)}_{W_O} \\
& + n \cdot \text{LN}(d) + n \cdot \underbrace{\text{Linear}(d, rd)}_{\text{up}} + n \cdot \underbrace{\text{Linear}(rd, d)}_{\text{down}}
\end{aligned} \tag{18}$$

where r is the FFN expansion ratio ($= 4$ for all models). Softmax, GELU, bias additions, and residual connections are omitted from both formulas and numerical totals. CanViT and DINOv3 use RoPE, adding $2n \cdot \text{RoPE_apply}(d)$ per block to rotate Q and K . Throughout, $+1$ terms in sequence lengths account for the CLS token.

G.3 CanViT-B

CanViT-B architecture parameters are in Table 1. Both glimpse grid and canvas grid are inference-time choices; the trained weights are independent of them. The breakdown below uses a 8×8 glimpse grid (64 patches) and 32×32 canvas grid. Token counts at this configuration:

- $N_{\text{local}} = 71$ (1 VPE + 1 CLS + 5 registers + 64 patches)
- $N_{\text{can}} = 1040$ (16 registers + 32^2 spatial tokens)

Per-glimpse cost (asymmetric projections, RoPE):

$$\begin{aligned}
C_{\text{glimpse}} = & \underbrace{\text{PatchEmbed}(N_p, p, d_{\text{bb}})}_{\text{backbone}} + L_{\text{bb}} \cdot \text{ViTBlock}(N_{\text{local}}, d_{\text{bb}}) \\
& + \underbrace{N_{\text{reads}} \cdot \text{CanvasRead}(N_{\text{local}}, N_{\text{can}}, d_{\text{bb}}, d_{\text{can}})}_{\text{canvas reads}} \\
& + \underbrace{N_{\text{writes}} \cdot \text{CanvasWrite}(N_{\text{local}}, N_{\text{can}}, d_{\text{bb}}, d_{\text{can}})}_{\text{canvas writes}}
\end{aligned} \tag{19}$$

$$C_{\text{total}}(T) = T \cdot (C_{\text{glimpse}} + C_{\text{seg}}) \tag{20}$$

where $C_{\text{seg}} = 32^2 \cdot \text{Linear}(d_{\text{can}}, 150)$ is a $\text{Conv}1 \times 1$ segmentation head on the spatial canvas tokens.

Table 10: CanViT per-glimpse cost breakdown (8×8 glimpse, 32×32 canvas, 71 local tokens, 1040 canvas tokens).

Component	Count	Each (G)	Total (G)
Patch embed + ViT blocks	1 + 12		12.3
Canvas Read	3	0.5	1.6
Canvas Write	3	0.5	1.6
Segmentation head	1	0.3	0.3
Per-glimpse total			15.9

G.3.1 Canvas Attention

Canvas Read (backbone queries canvas, asymmetric projections):

$$\begin{aligned}
\text{CanvasRead}(n_l, n_c, d_l, d_c) = & n_l \cdot \text{LN}(d_l) + n_c \cdot \text{LN}(d_c) \\
& + \underbrace{n_l \cdot \text{Linear}(d_l, d_c)}_{W_Q} \\
& + n_l \cdot \text{RoPE_apply}(d_c) + n_c \cdot \text{RoPE_apply}(d_c) \\
& + \text{SDPA}(n_l, n_c, d_c) + \underbrace{n_l \cdot \text{Linear}(d_c, d_l)}_{W_O}
\end{aligned} \tag{21}$$

Canvas tokens serve as K and V after LN, without learned projection.

Canvas Write (canvas queries backbone):

$$\begin{aligned} \text{CanvasWrite}(n_l, n_c, d_l, d_c) &= n_c \cdot \text{LN}(d_c) + n_l \cdot \text{LN}(d_l) \\ &\quad + \underbrace{2n_l \cdot \text{Linear}(d_l, d_c)}_{W_K, W_V} \\ &\quad + n_c \cdot \text{RoPE_apply}(d_c) + n_l \cdot \text{RoPE_apply}(d_l) \\ &\quad + \text{SDPA}(n_c, n_l, d_c) \end{aligned} \tag{22}$$

Canvas tokens serve as Q after LN, without learned projection (W_O omitted). Both Canvas Read and Canvas Write apply SR-RoPE.

G.4 DINOv3 ViT-B Teacher

Table 11: DINOv3 ViT-B architecture.

Parameter	Value
d	768
L	12
p	16
N_{regs}	4
RoPE	yes

For resolution $R \times R$:

$$\begin{aligned} C_{\text{teacher}}(R) &= \text{PatchEmbed}((R/p)^2, p, d) \\ &\quad + L \cdot \text{ViTBlock}(1 + N_{\text{regs}} + (R/p)^2, d) \end{aligned} \tag{23}$$

Quadratic attention makes this $O(R^4)$.

At $R = 512$: $N = 1 + 4 + 32^2 = 1029$ tokens, yielding ≈ 215.2 GFLOPs.

G.5 AME (Attention-Map Entropy)

AME²³ uses a MAE-style architecture with sinusoidal positional embeddings (no RoPE).

Table 12: AME architecture²³ (Section 4.1).

Parameter	Encoder	Decoder
d	1024	512
Depth	24	8
Backbone	ViT-L	—
Image size	128 × 256	
Patch size	16	
Patches/glimpse	9 (3×3)	
Total patches	128	

The encoder re-processes *all* accumulated patches at each step (at step t , the encoder sees $g \cdot (t + 1)$ patches from glimpses 0 through t). The decoder processes all $N_{\text{patches}} + 1 = 129$ tokens at every step: 128 patch positions (visible embeddings from the encoder, learnable mask tokens for unseen positions) plus one CLS token. “Head” denotes the per-patch prediction head ($N_{\text{patches}} \cdot \text{Linear}(d_{\text{dec}}, p^2 \cdot \text{num_classes})$).

$$C_{\text{AME}}(T) = \sum_{t=0}^{T-1} [\text{PatchEmbed}(g \cdot (t+1), p, d_{\text{enc}}) + L_{\text{enc}} \cdot \text{ViTBlock}(g \cdot (t+1) + 1, d_{\text{enc}})]_{24} \\ + (T+1) \cdot [L_{\text{dec}} \cdot \text{ViTBlock}(N_{\text{patches}} + 1, d_{\text{dec}}) + \text{Head}]$$

Re-encoding all accumulated patches yields $O(T^2)$ total encoder cost.

Table 13: AME cost at $T = 8$ glimpses.

Component ($T = 8$)	GFLOPs
Encoder (cumulative re-encoding)	202.8
Decoder ($9 \times$)	106.2
Total	309.0

Note on PatchEmbed: AME and AdaGlimpse use MAE-style patch embedding, where a conv2d runs on the *entire* image at every step, not just the newly revealed patches. Our formula conservatively counts only the visible patches at each step (i.e., $\text{PatchEmbed}(g \cdot t, \dots)$ instead of $\text{PatchEmbed}(N_{\text{patches}}, \dots)$). This underestimates the true cost by ≈ 1.1 G over 8 glimpses ($< 0.4\%$), making AME appear slightly more efficient.

G.6 AdaGlimpse

AdaGlimpse²⁴ uses a MAE-style architecture with a CNN upsampling head and sinusoidal positional embeddings (no RoPE). Like AME, the encoder re-processes accumulated patches.

Table 14: AdaGlimpse architecture²⁴ (Section 4).

Parameter	Encoder	Decoder
d	768	512
Depth	12	8
Backbone	ViT-B	—
Image size	224×224	
Patch size	16	
Patches/glimpse	9 (3×3)	
Total patches	196	
CNN head	—	6 layers ($14 \times 14 \rightarrow 224 \times 224$)

$$C_{\text{AdaGlimpse}}(T) = \sum_{t=0}^{T-1} [\text{PatchEmbed}(g \cdot (t+1), p, d_{\text{enc}}) + L_{\text{enc}} \cdot \text{ViTBlock}(g \cdot (t+1) + 1, d_{\text{enc}})]_{25} \\ + (T+1) \cdot [L_{\text{dec}} \cdot \text{ViTBlock}(N_{\text{patches}} + 1, d_{\text{dec}}) + \text{CNN}]$$

Table 15: AdaGlimpse cost at $T = 8$ glimpses. The same PatchEmbed caveat as AME applies.

Component ($T = 8$)	GFLOPs
Encoder (cumulative re-encoding)	57.4
Decoder — ViT (9×10.6)	95.4
Decoder — CNN (9×84.3)	758.7
Total	911.3

G.7 Summary

Table 16: Total FLOPs at representative operating points.

Model	Encoder (G)	Decoder (G)	Total (GFLOPs)
CanViT ($T = 1$)	12.3	3.2	15.9
DINOv3 ViT-B (512 × 512)	—	—	215.2
AME ($T = 8$)	202.8	106.2	309.0
AdaGlimpse ($T = 8$)	57.4	853.9	911.3

Architecture parameters for AME and AdaGlimpse are sourced from the respective papers (AME: Pardy et al.²³ Table 3; AdaGlimpse: Pardy et al.²⁴ Table 3) and cross-checked against their public codebases (github.com/apardyl/AME, github.com/apardyl/AdaGlimpse).

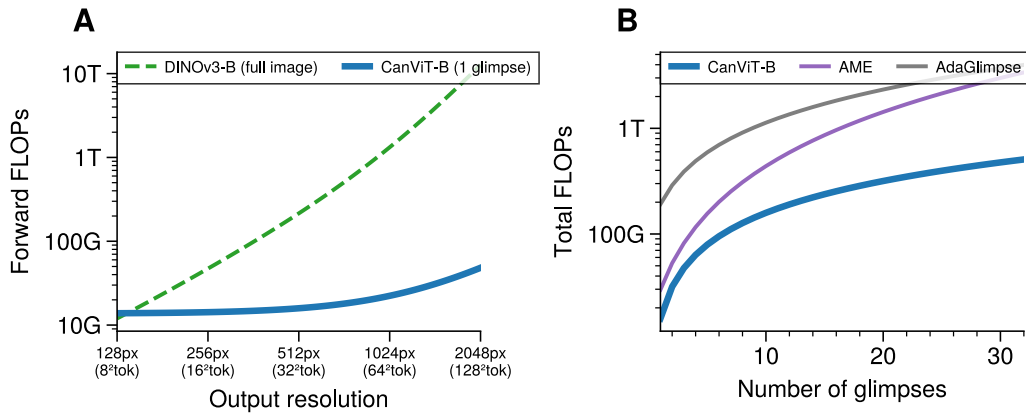


Figure 7: **Analytical FLOP scaling.** All curves computed from the formulas in Section G. **(A)** FLOPs for a single inference step vs. output resolution (canvas grid² tokens for CanViT, image grid² for DINOv3). CanViT’s backbone processes a fixed-size glimpse; Canvas Attention cost grows with output resolution. **(B)** Total FLOPs vs. number of glimpses at fixed output resolution. CanViT cost is linear in T ; AME and AdaGlimpse re-encode all accumulated patches at each step ($\mathcal{O}(T^2)$ encoder cost).

H DINOv3 ImageNet-1K Linear Classification Probes

We evaluate a frozen DINOv3 baseline using linear probing on ImageNet-1k. However, upon its release, DINOv3 provided a pretrained ImageNet-1k linear classification head only for the 7B-parameter flagship model. The smaller ViT checkpoints (ViT-S/16, ViT-S+/16, ViT-B/16, ViT-L/16, ViT-H+/16) shipped without IN1k probes, and only ImageNet-ReAL top-1 accuracy was reported²⁸ (Table 14), not raw IN1k top-1.

We trained and released linear probes for all five smaller DINOv3 ViT models. All of our probes match or exceed the best IN1k-ReAL top-1 validation accuracy reported by the DINOv3 authors. Our trained probes are publicly available at <https://github.com/yberreby/dinov3-in1k-probes>.

H.1 Feature Extraction

We extract CLS tokens from the last transformer layer of each DINOv3 ViT model at 512×512 input resolution (1024 patch tokens with 16 × 16 px patches), using bfloat16 automatic mixed precision for the forward pass. CLS tokens are stored in float32.

Data loading uses Inception-crop augmentation for the training split.

Features are pre-computed and cached to disk before any probe training begins. This decouples the expensive backbone forward pass from the probe optimization, which iterates over cached feature vectors rather than running the backbone or loading images. This makes extensive hyperparameter search over the full training set practical.

Since augmentation is applied at extraction time and baked into the cached features, each extraction run through the training split (with different random shuffling and augmentation) produces a separate file. To train with N augmentation epochs, N extraction passes must be run and stored. During probe training, each file is treated as an independent epoch.

H.2 Probe Architecture

The probe is a single linear layer (`nn.Linear`) mapping from the model’s embedding dimension to 1000 ImageNet classes, with bias.

H.3 Hyperparameter Optimization

Hyperparameters are tuned using Optuna, maximizing ImageNet-ReAL top-1 validation accuracy.

The search space includes:

- Optimizer: AdamW or SGD (categorical)
- Reference learning rate: 10^{-7} to 10^{-2} (log-uniform distribution), scaled linearly by batch size
- Batch size: powers of 2, from `max_batch_size/4` to `max_batch_size`
- For AdamW: weight decay (0 to 0.1), β_1 (0.1 to 0.99, log-uniform), β_2 (derived from β_1 via gap fraction parameterization)
- For SGD: momentum (0 to 0.99)
- Weight initialization: DINOv3-style (weights $\sim \mathcal{N}(0, 0.01)$, bias = 0) or PyTorch default (categorical)

Learning rate schedule: linear warmup over 10% of total steps, followed by cosine annealing to 0.

Peak learning rate is computed as `ref_lr × batch_size` (linear scaling rule).

Trials are pruned early if validation loss exceeds the initial (untrained) loss, preventing wasted compute on clearly divergent runs.

H.4 Loss Functions

Two loss functions are supported:

- Standard softmax cross-entropy (single-label)
- Sigmoid cross-entropy⁶³ treating each class as independent binary classification.

H.5 Evaluation

Validation is performed after each training epoch using both:

- Standard ImageNet-1k top-1 and top-5 accuracy
- ImageNet-ReAL top-1 accuracy⁶³, which accounts for multi-label ground truth

H.6 Published Results

Table 17: DINOv3 IN1k linear probe accuracy at 512×512 resolution. All probes match or exceed the official ReAL top-1 numbers from the DINOv3 paper (Table 14).

Model	IN-ReAL top-1 (official / ours)	IN1k top-1 (ours)
ViT-S/16	87.0% / 87.08%	81.40%
ViT-S+/16	88.0% / 88.08%	82.89%
ViT-B/16	89.3% / 89.54%	85.00%
ViT-L/16	90.2% / 90.42%	87.44%
ViT-H+/16	90.3% / 90.31%	87.65%

Table 18: Selected hyperparameters for each DINOv3 linear probe, found via Optuna.

Model	Loss	Batch size	Peak LR	Weight decay	(β_1, β_2)	DINOv3 init	Aug. epochs	Total epochs
ViT-S/16	softmax	2048	6.6×10^{-3}	6.0×10^{-2}	(0.22, 0.71)	Yes	10	20
ViT-S+/16	softmax	1024	1.1×10^{-3}	3.8×10^{-2}	(0.10, 0.94)	No	10	20
ViT-B/16	softmax	1024	2.8×10^{-4}	9.2×10^{-2}	(0.56, 0.73)	Yes	10	20
ViT-L/16	sigmoid	2048	3.0×10^{-3}	3.1×10^{-2}	(0.40, 0.63)	Yes	10	20
ViT-H+/16	sigmoid	1024	8.2×10^{-3}	4.9×10^{-2}	(0.78, 0.93)	No	8	16

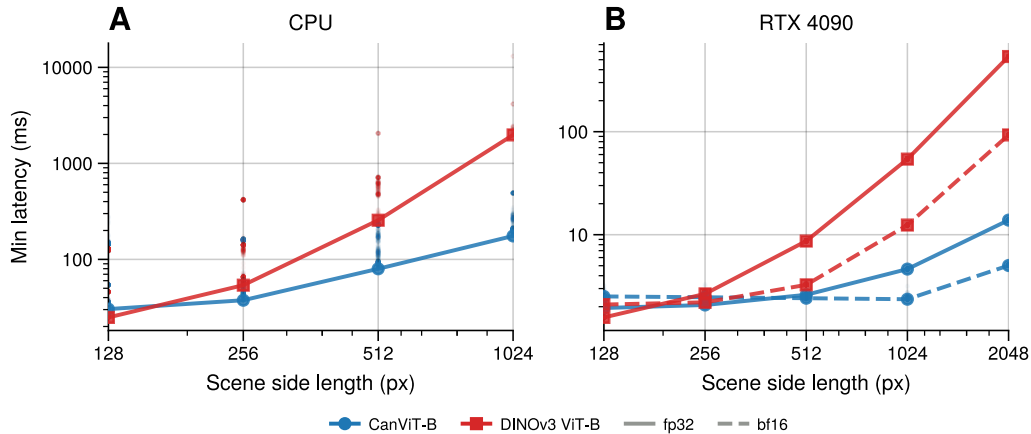


Figure 8: **Real-time latency: CanViT-B vs DINOv3 ViT-B/16.** Minimum per-forward-pass latency ($B = 1$, with device sync) across scene side lengths. CPU: best of 1–32 thread configurations; CUDA: torch.compile, fp32 and AMP bf16. Faint dots: all raw timings. Solid markers: minimum. Full breakdown in Table 19.

I Inference Latency Experiments

I.1 Benchmarking Protocol

We measure per-forward-pass *latency* (not throughput): each timed iteration processes a single input ($B = 1$) with explicit device synchronization before and after.

Warmup. We run 3 warmup iterations before measurement (excluded from the time budget). The first iteration triggers torch.compile graph capture and kernel compilation. Peak GPU memory is measured after warmup.

Measurement. We then run timed iterations for a fixed time budget (60 seconds for CUDA, 30 for CPU), recording the elapsed time of each individual forward pass. All raw per-iteration timings are preserved for downstream analysis.

Hardware. CUDA benchmarks use NVIDIA GeForce RTX 4090. CPU benchmarks include both single-threaded (torch.set_num_threads(1)) and multi-threaded (4, 8, 16, 32 threads) configurations.

Precision. We benchmark CUDA in both float32 and AMP bfloat16 (torch.autocast) to isolate the effect of mixed precision. CPU benchmarks use float32.

Compilation. CUDA benchmarks use torch.compile (fullgraph mode). CPU benchmarks run in eager mode.

I.2 Results

Figure 8 compares the per-forward-pass latency of CanViT-B and DINOv3 ViT-B/16 across scene resolutions. CanViT’s backbone always processes a fixed 128×128 px glimpse; only Canvas Attention scales with output resolution (canvas grid size). DINOv3 processes all $(s/16)^2$ patches in a single forward pass, scaling quadratically. On CUDA, CanViT’s overhead is negligible up to 1024^2 px scenes; on CPU, the scaling is more pronounced but CanViT remains substantially faster at high resolutions.

Table 19: **Inference latency ($B = 1$, per-forward-pass sync, min of $n \geq 50$ iters).** See Section I.1 for full protocol. nT = number of CPU threads (`torch.set_num_threads`). Bold = faster model (latency) or lighter (memory) at matched output resolution (canvas grid = scene px /16 for CanViT, patch grid = input px /16 for DINOv3). Speedup = $t_{\text{DINOv3}}/t_{\text{CanViT}}$.

Device	Scene (px)	CanViT-B		DINOv3 ViT-B/16		Speedup
		ms	MB	ms	MB	
Ryzen 7950X (1T)	128	143	—	123	—	0.9×
Ryzen 7950X (1T)	256	154	—	413	—	2.7×
Ryzen 7950X (1T)	512	224	—	2048	—	9.1×
Ryzen 7950X (1T)	1024	488	—	13065	—	26.8×
Ryzen 7950X (4T)	128	54	—	45.8	—	0.8×
Ryzen 7950X (4T)	256	59.9	—	141	—	2.4×
Ryzen 7950X (4T)	512	90.7	—	700	—	7.7×
Ryzen 7950X (4T)	1024	201	—	4141	—	20.6×
Ryzen 7950X (8T)	128	30.9	—	26.4	—	0.9×
Ryzen 7950X (8T)	256	37.5	—	65.4	—	1.7×
Ryzen 7950X (8T)	512	79.8	—	451	—	5.7×
Ryzen 7950X (8T)	1024	175	—	2333	—	13.3×
Ryzen 7950X (16T)	128	30.4	—	24.9	—	0.8×
Ryzen 7950X (16T)	256	39	—	108	—	2.8×
Ryzen 7950X (16T)	512	101	—	589	—	5.8×
Ryzen 7950X (16T)	1024	180	—	1978	—	11×
Ryzen 7950X (32T)	128	35.7	—	26.1	—	0.7×
Ryzen 7950X (32T)	256	42	—	53.9	—	1.3×
Ryzen 7950X (32T)	512	143	—	256	—	1.8×
Ryzen 7950X (32T)	1024	233	—	2152	—	9.2×
NVIDIA GeForce RTX 4090 (AMP bf16)	128	2.52	397	2.1	359	0.8×
NVIDIA GeForce RTX 4090 (AMP bf16)	256	2.47	402	2.21	362	0.9×
NVIDIA GeForce RTX 4090 (AMP bf16)	512	2.42	419	3.26	388	1.3×
NVIDIA GeForce RTX 4090 (AMP bf16)	1024	2.36	499	12.4	416	5.3×
NVIDIA GeForce RTX 4090 (AMP bf16)	2048	5.02	794	93	607	18.5×
NVIDIA GeForce RTX 4090 (fp32)	128	1.94	395	1.57	356	0.8×
NVIDIA GeForce RTX 4090 (fp32)	256	2.08	408	2.66	359	1.3×
NVIDIA GeForce RTX 4090 (fp32)	512	2.61	430	8.68	378	3.3×
NVIDIA GeForce RTX 4090 (fp32)	1024	4.64	544	54.2	454	11.7×
NVIDIA GeForce RTX 4090 (fp32)	2048	13.9	996	537	758	38.7×